



OPEN

Discovery and molecular basis of subtype-selective cyclophilin inhibitors

Alexander A. Peterson^{1,2,3,8}, Aziz M. Rangwala^{4,8}, Manish K. Thakur⁴, Patrick S. Ward^{5,6,7}, Christie Hung^{1,2,3}, Ian R. Outhwaite⁴, Alix I. Chan^{1,2,3}, Dmitry L. Usanov^{1,2,3}, Vamsi K. Mootha^{5,6,7}, Markus A. Seeliger⁴✉ and David R. Liu^{1,2,3}✉

Although cyclophilins are attractive targets for probing biology and therapeutic intervention, no subtype-selective cyclophilin inhibitors have been described. We discovered novel cyclophilin inhibitors from the in vitro selection of a DNA-templated library of 256,000 drug-like macrocycles for cyclophilin D (CypD) affinity. Iterated macrocycle engineering guided by ten X-ray co-crystal structures yielded potent and selective inhibitors (half maximal inhibitory concentration (IC₅₀) = 10 nM) that bind the active site of CypD and also make novel interactions with non-conserved residues in the S2 pocket, an adjacent exo-site. The resulting macrocycles inhibit CypD activity with 21- to >10,000-fold selectivity over other cyclophilins and inhibit mitochondrial permeability transition pore opening in isolated mitochondria. We further exploited S2 pocket interactions to develop the first cyclophilin E (CypE)-selective inhibitor, which forms a reversible covalent bond with a CypE S2 pocket lysine, and exhibits 30- to >4,000-fold selectivity over other cyclophilins. These findings reveal a strategy to generate isoform-selective small-molecule cyclophilin modulators, advancing their suitability as targets for biological investigation and therapeutic development.

The human cyclophilin family consists of 17 proteins containing a structurally conserved peptidyl-prolyl-isomerase (PPIase) domain¹. At least 12 members of this family catalyze the *cis-trans* isomerization of peptidyl-proline bonds^{1,2}, a rate-limiting step in the folding of many proteins^{3,4}. Cyclophilin D (CypD) is unique as a mitochondrial cyclophilin^{1,3} and a key regulator of the mitochondrial permeability transition pore (mPTP), a transient channel on the inner mitochondrial membrane that opens under oxidative stress or high mitochondrial matrix calcium levels^{5–8}. Inhibition^{5,6,8,9} or knockout^{5–8} of CypD causes the mPTP to be more resistant to pore opening events. Prolonged mPTP opening causes osmotic imbalance, mitochondrial swelling and rupture, and cell death^{7,8,10}. This pathway has been implicated in a variety of conditions associated with oxidative stress, including ischemia-reperfusion injury (IRI)^{8,11}, many neurodegenerative disorders^{12–18}, liver diseases¹⁹, aging and autophagy^{20,21}, and diabetes²². Inhibition of CypD is thus considered a potential therapeutic strategy for IRI^{7,8}, Alzheimer's disease¹³, Huntington's disease¹⁴, multiple sclerosis¹⁶, Parkinson's disease¹⁸, amyotrophic lateral sclerosis¹², X-linked adrenoleukodystrophy¹⁷, liver cirrhosis¹⁹, and diabetes-related diseases²². While the exact structure^{23–25}, function^{5,10,20}, and regulatory pathways^{5,10} of the mPTP are still debated, CypD is a well-established regulator of mPTP function. CypD inhibitors could therefore also illuminate other protein regulators and structural components of the mPTP.

While inhibiting CypD is attractive for studying the mPTP and for treating conditions linked to oxidative stress, the 16 other known cyclophilin isoforms play diverse and important biological roles^{3,4,26–29}. Cyclophilin subtype selectivity is therefore critical

for biological probes and for potential therapeutics to minimize unwanted side-effects from off-target cyclophilin perturbation. To our knowledge, no subtype-selective cyclophilin inhibitors have been described for any cyclophilin isoforms^{1,3}. Efforts to develop selective cyclophilin inhibitors are stymied by the high sequence identity (61–86%) and highly conserved structures of human PPIase domains¹.

A key structural feature shared among all cyclophilin isoforms is a shallow and highly conserved PPIase active site^{1,30} (Extended Data Fig. 1a,b). Classic cyclophilin inhibitors such as cyclosporine A (CsA) bind to this active site^{1,30} and thus equipotently inhibit most cyclophilins (Extended Data Fig. 1a,c and Supplementary Fig. 1). Adjacent to the active site is the S2 pocket, a distinct exo-site that forms part of a long substrate-binding groove for peptides (Extended Data Fig. 1a). S2 pocket residues are much more diverse than active site residues among cyclophilins, providing an opportunity for isoform-selective binding¹ (Extended Data Fig. 1d). In particular, three gatekeeper residues (positions 123, 124, and 145 in CypD) and one far S2 pocket residue (position 118 in CypD) are highly diverse among cyclophilins (Extended Data Fig. 1e). While S2 pocket binding has been recognized as a strategy to achieve isoform-selective inhibition¹, current small-molecule cyclophilin inhibitors when profiled show poor isoform selectivity and are not known to exploit interactions with non-conserved S2 exo-site residues^{3,30–37}.

In this study we report the development of novel cyclophilin inhibitors from a DNA-templated macrocycle library and iterated structural biology and small-molecule engineering, yielding potent and isoform-selective CypD and CypE inhibitors. These findings establish a strategy for the development of subtype-selective

¹Merkin Institute of Transformative Technologies in Healthcare, Broad Institute of MIT and Harvard, Cambridge, MA, USA. ²Department of Chemistry and Chemical Biology, Harvard University, Cambridge, MA, USA. ³Howard Hughes Medical Institute, Harvard University, Cambridge, MA, USA.

⁴Department of Pharmacological Sciences, Stony Brook University, Stony Brook, NY, USA. ⁵Broad Institute of MIT and Harvard, Cambridge, MA, USA.

⁶Howard Hughes Medical Institute and Departments of Molecular Biology and Medicine, Massachusetts General Hospital, Boston, MA, USA.

⁷Department of Systems Biology, Harvard Medical School, Boston, MA, USA. ⁸These authors contributed equally: Alexander A. Peterson, Aziz M. Rangwala.

✉e-mail: markus.seeliger@stonybrook.edu; drliu@fas.harvard.edu

cyclophilin modulators through engineering interactions with unique S2 pocket exo-site residues.

Results

Selection of a library of 256,000 DNA-templated macrocycles.

To identify new cyclophilin inhibitors in an unbiased manner, we performed the selection of a DNA-templated library of 256,000 macrocycles³⁸ for binding immobilized CypD. Analysis of selection data revealed a highly conserved group of putative cyclophilin binders: the JO** family, where each letter identifies a library building block at one of the four macrocycle positions, and * indicates broad structural variation (Extended Data Fig. 2a). A set of highly enriched macrocycles was synthesized in DNA-free form as both the *cis* (ending in *c*) and *trans* (ending in *t*) olefin isomers, then assayed for their ability to inhibit cyclophilin prolyl isomerization on a peptide substrate (succinate-AAPF-AMC). Two library hits show modest inhibition of CypD prolyl-isomerase activity, JOMBt (half maximal inhibitory concentration (IC_{50}^{CypD}) = 17 μ M) and JOBBt (IC_{50}^{CypD} = 45 μ M) (Fig. 1a and Extended Data Fig. 2b,c). These results were verified by surface plasmon resonance, which yielded dissociation constants of: JOMBt K_D^{CypD} = 19 μ M and JOBBt K_D^{CypD} = 45 μ M (Supplementary Fig. 2a–c). Other strongly enriched hits from this selection include HOJt/c and HJJt/c, which show no prolyl-isomerase inhibition for either isomer (Extended Data Fig. 2b) and may bind CypD without inhibiting PPI activity.

We used JOMBt as a scaffold to reveal structure–activity relationships and improve potency against CypD (Fig. 1a and Extended Data Fig. 2c; A series). The synthesis and evaluation of 48 JOMBt analogs revealed several key insights, including a highly conserved first-position 1J building block (A1–A6), stereochemistry and an aromatic moiety requirement at the second building block (A7–A20), certain piperidine cyclohexane structures with specific connectivity and stereochemistry at the third building block (A21–A29, JOGBt/c-A, JOCBt/c-A, JOGAt/c), preferred diamino-butyric acid derivatives at the fourth building block (JOMAt/c, JOMCt/c, JOMFt/c, JOGAt/c), required fumarate-like macrocycle linker (A30, JOMBc, JOBBc), and no preference for a series of tail moieties (JOMBtA, JOMBtD) (Fig. 1a and Extended Data Fig. 2c).

Adding a benzyl group to the tertiary carbon in the piperidine ring of JOMBt (resulting in A26) increases CypD potency 85-fold to IC_{50}^{CypD} = 0.20 μ M (Extended Data Fig. 2c). We assayed compounds against a full panel of 11 cyclophilins with prolyl-isomerase activity (Supplementary Fig. 3a) to assess subtype selectivity. JOMBt and A26 show promiscuous cyclophilin inhibition (Fig. 1b,c and Supplementary Fig. 4a,c), similar to that of CsA (Extended Data Fig. 1c).

Co-crystal structures reveal inhibitor binding mode. To illuminate the molecular basis of CypD inhibition by JOMBt and A26 we solved X-ray co-crystal structures of each compound bound to CypD (Fig. 1d–f and Extended Data Fig. 3a–c, Protein Data Bank (PDB) IDs 7TGS, 7TGT). Both compounds share a similar binding mode, with the phenyl ring of the 1J building block anchoring the macrocycle in the hydrophobic pocket of the active site, supplemented with key hydrogen bonding interactions between the macrocycle backbone and active site residues (Fig. 1d,e and Extended Data Fig. 3a). A26 engages CypD more extensively than JOMBt. The benzyl group of A26 engages in hydrophobic contacts with T115 (Extended Data Fig. 3b), while the macrocycle backbone forms a closer hydrogen bond with the side-chain N–H on W163 (Extended Data Fig. 3c). While this benzyl group increases potency, it does not influence CypD selectivity, likely owing to hydrophobic contacts with semi-conserved S2 pocket residue T115 in other cyclophilins (Extended Data Fig. 1d). Indeed, replacing the benzyl group with –H (JOMBt) or –Me (A25) resulted in almost identical selectivity profiles (Supplementary Fig. 4a–c).

Both crystal structures revealed very shallow placement of the furan building block just inside the S2 pocket (Fig. 1f and Extended Data Fig. 3a,b). Given our hypothesis that S2 pocket engagement could yield subtype selectivity, we reasoned that replacing this furan with other groups might increase CypD selectivity. Consistent with this possibility, macrocycle A14, in which the furan of JOMBt is replaced with a benzophenone, shows increased selectivity over CypG, CypH, and NKTR (Supplementary Fig. 4d).

S2 pocket ligands influence CypD selectivity and potency.

Encouraged by the above results, we synthesized a new series of macrocycles (B series) using A26 as a scaffold, varying potential S2-binding groups to increase CypD selectivity. Large hydrophobic groups that replace the furan in A26, such as benzophenone B1 (IC_{50}^{CypD} = 0.040 μ M) or biphenyl B2 (IC_{50}^{CypD} = 0.18 μ M), retain CypD potency, but no longer potently inhibit NKTR, CypH, or CypG, with some selectivity over PPWD1 (Fig. 2a,b and Supplementary Fig. 5a,b). The S2 pockets in these cyclophilins are more sterically occluded or rigid than in the other seven tested cyclophilins, likely clashing with large hydrophobic moieties in B1 and B2 (Fig. 2d). To gain further insight into the basis of emerging CypD subtype selectivity, we solved co-crystal structures of B1, B2, and a smaller derivative B3 bound to CypD (Fig. 2c and Supplementary Fig. 5c; PDB IDs 7TGU, 7TGV, 7TH1). These structures revealed deeper S2 pocket binding by the benzophenone and biphenyl groups of B1 and B2, respectively, while retaining the original active site interactions of the parent compound A26. We also observed migration of the R124 side-chain contingent on the size of the S2-binding moiety. As the ligand grew in size from B3 → B2 → B1, the R124 side-chain gradually moved from tucked in the pocket to fully solvent-exposed (Fig. 2c and Supplementary Fig. 5c).

These observations suggest the need to displace some residues within the S2 pocket during ligand binding to achieve partial CypD subtype selectivity. While the polarity and hydrophilicity of R124 in CypD minimizes the energetic cost of doing so, CypG, CypH, NKTR, and PPWD1 contain large hydrophobic groups or inflexible residues buried in the S2 pocket, and moving their side-chains out of the pocket would likely incur a large energetic penalty (Fig. 2d). This observation was supported by additional macrocycles for which the largest, most hydrophobic derivatives (such as B5) are more selective for CypD than smaller or more hydrophilic analogs (B4, B6, B7) (Supplementary Fig. 6a–d).

To further improve selectivity for CypD, we diversified the biphenyl ring of B2, which was positioned in our co-crystal structures near K118, S123 and R124 within CypD's S2 pocket. We reasoned that establishing favorable interactions with these residues might further improve subtype selectivity. While derivatives that contain various alkyl, alkoxy, phenols, or heterocycles at varying positions on the distal ring of the biphenyl (B8–B14) provide no additional benefit, these biphenyl derivatives maintain the same selectivity profile as B2 (Supplementary Fig. 7a–g). We also observed that *para*-carbonyl moieties, such as B15 (IC_{50}^{CypD} = 0.038 μ M), show promising potency with a preference of 2- to 20-fold for CypD over CypC and Cyp40 (B15–B19; Supplementary Fig. 8a–e). Replacement of the acetyl group of B15 with a carboxylate resulted in a tenfold decrease in CypD potency (B20, IC_{50}^{CypD} = 0.3 μ M; Supplementary Fig. 9a) but drastically improved selectivity over CypC and Cyp40 to at least ninefold. This trend was also observed in a closely related analog (B21, IC_{50}^{CypD} = 0.17 μ M; Supplementary Fig. 9b; PDB ID 7TH6).

Potency against CypD was rescued upon distancing the carboxylate from the biphenyl group by one or two carbons (B22, IC_{50}^{CypD} = 0.04 μ M; B23, IC_{50}^{CypD} = 0.0078 μ M; Fig. 3a,b and Supplementary Fig. 9c,d). B23 shows a dramatic improvement in subtype selectivity, with >500-fold selectivity over CypC, Cyp40, PPWD1, CypH, CypG, NKTR, 25- to 40-fold selectivity over CypA and PP1L1, and ~3-fold selectivity over CypE and CypB. Changing

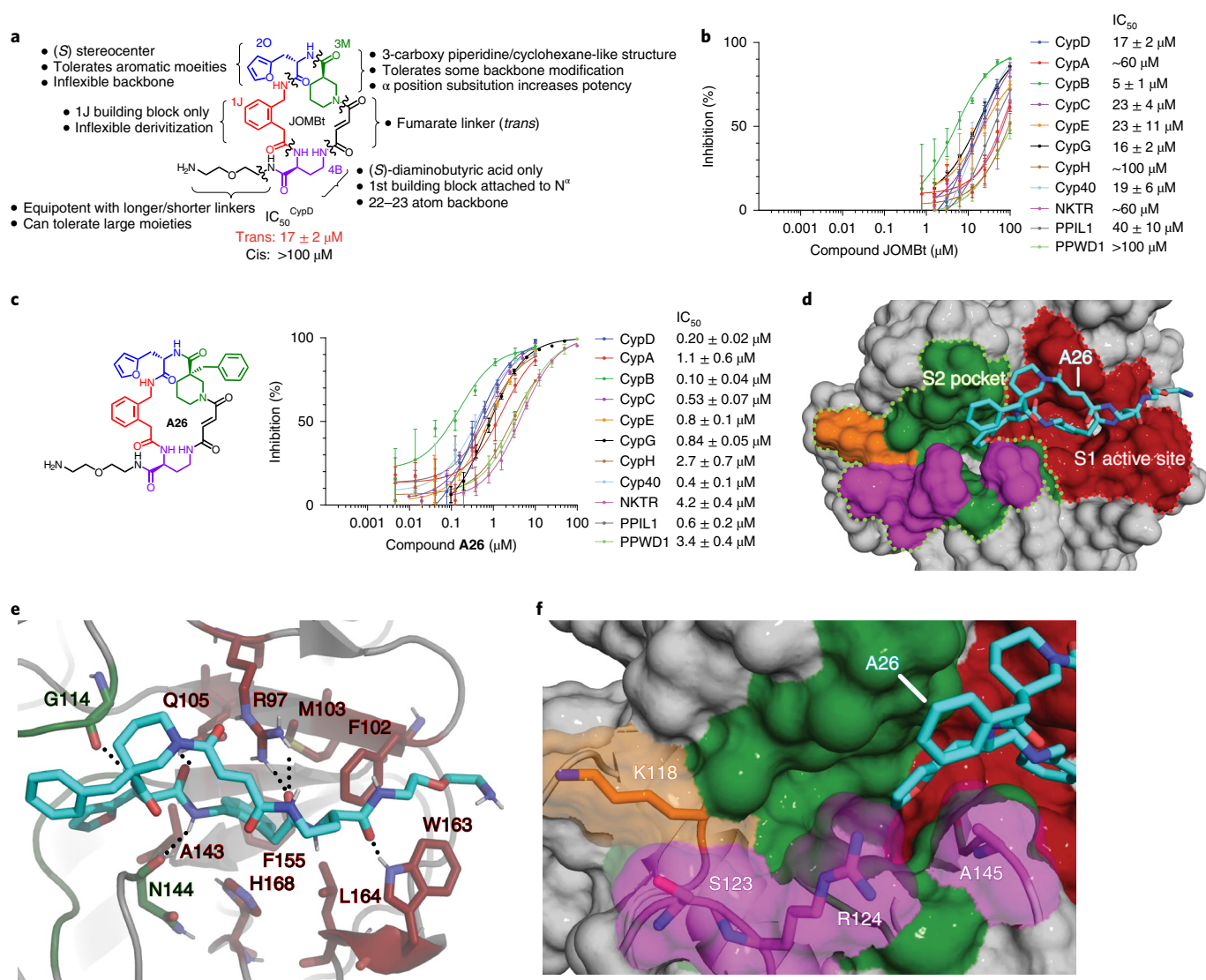


Fig. 1 | Selection of a DNA-templated library of 256,000 macrocycles for CypD affinity reveals novel cyclophilin inhibitors. **a**, Generalized trends in inhibition potency of CypD prolyl-isomerase activity from cyclophilin inhibition profiles of library hits and **A**-series macrocycles. **b**, JOMBt, showing weak and promiscuous cyclophilin inhibition of prolyl-isomerase activity. **c**, Compound **A26** showing improved CypD potency but promiscuous inhibition. **d**, X-ray co-crystal structure of compound **A26** (cyan) bound to CypD (PDB ID 7TGT, 1.06 Å resolution), shown as a space-filling model. **A26** has a dual-binding mode involving the active site (red) and S2 pocket (green) of CypD. **e**, Active site binding interactions with **A26**. The phenyl group provides the primary hydrophobic interactions with F102, M103, A143, F155, L164, and H168. Black dashes show predicted hydrogen bonding interactions with R97, Q105, G114, N144, and W163 and the backbone of the **A26**. **f**, S2 pocket binding pose of the furan of **A26**, exhibiting a shallow interaction that does not engage non-conserved residues K118 (orange), S123 (magenta), and R124 (magenta) on the far side of the pocket. IC₅₀ values reflect mean ± s.e.m. of three technical replicates. Data points and error bars reflect mean ± s.d. of individual assays at one dose.

the carboxylate linker to a vinyl group (**B24**, IC₅₀^{CypD} = 0.0019 μM; Supplementary Fig. 9e) or ethynyl group (**B25**, IC₅₀^{CypD} = 0.0030 μM; Fig. 3a,b and Supplementary Fig. 9f) results in potency and selectivity profiles that are similar to **B23**. The selectivity and potency of these carboxylates are attenuated upon migrating the position of the carboxylate (**B26**, **B27**; Supplementary Fig. 10a,b), or masking the negative charge of the carboxylate through an ester or nitro group (**B28–B30**) (Supplementary Fig. 10c–e). Replacing the carboxylate with an amine results in a 500- to 1,000-fold reduction in potency for CypD, and a changed selectivity profile that favors PPWD1 and CypC (**B31**, **B32**) (Supplementary Fig. 11a, b). Nitriles **B33** and **B34** also exhibit a similar linker-length-dependent potency profile, with **B34** showing similar potency to **B23**, yet with reduced selectivity (Supplementary Fig. 12a,b). Collectively, these results suggest that carboxylate-containing biphenyl-substituted inhibitors gain CypD

potency though a novel interaction that is both charge selective and hydrogen-bond dependent. Moreover, **B23**, **B24**, and **B25** establishes that iterative diversification deeper into the S2 pocket with precisely tailored chemical properties can result in enhanced selectivity for CypD.

Structural and mutagenesis studies improve CypD selectivity. We solved a co-crystal structure of **B23** or **B25** bound to CypD (Fig. 3c; PDB IDs 7TH7 and 7THC). While retaining the same interactions with CypD as **B2**, we also observed a novel hydrogen bond with the backbone of S119 and a salt bridge with the side-chain of K118, which is usually oriented away from the S2 pocket (Extended Data Fig. 4a). The latter interaction explains why cyclophilins that replace the K118 residue with a glutamate (Cyp40, PPWD1), or a hydrophobic residue (CypC, PPIL1) are much less potently inhibited by **B23**

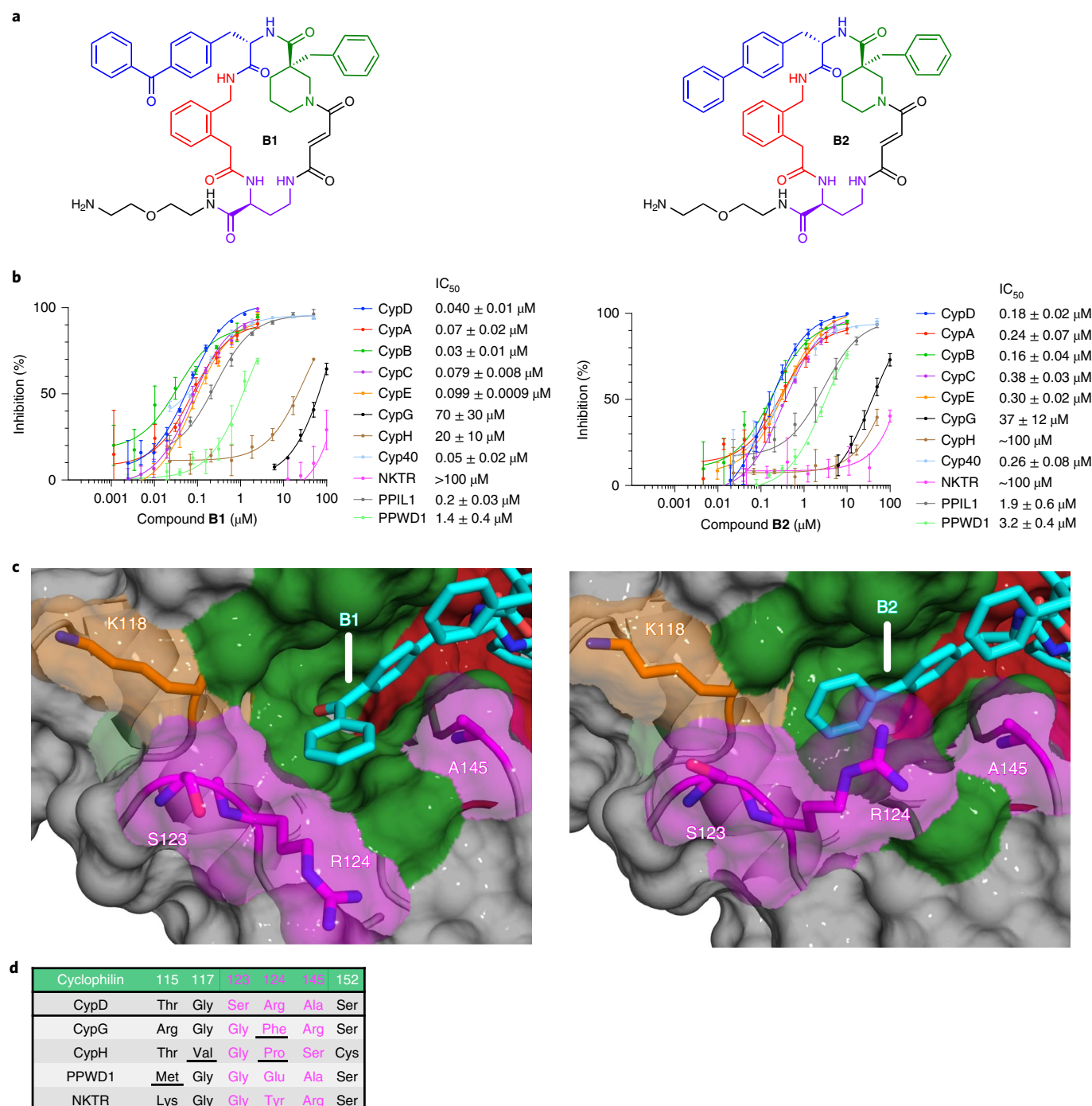


Fig. 2 | Compounds with large S2 pocket binding groups show reduced potency against cyclophilins with sterically occluded S2 pockets. **a**, Structure of **B1**, **B2**. **b**, Cyclophilin prolyl-isomerase inhibition screens for **B1** and **B2**. **c**, Co-crystal structures of **B1** (PDB ID 7TGU, 1.21 Å resolution) or **B2** (PDB ID 7TGV, 1.46 Å resolution) bound to CypD, viewing the S2 pocket. Active site binding is identical to that of **A26** (Fig. 1e). **d**, Residues within the S2 pocket of cyclophilins inhibited less potently by **B1** and **B2**, with important residues underlined. The benzophenone or biphenyl group of **B1** or **B2**, respectively, fills the S2 pocket more completely, resulting in selectivity over cyclophilins with more sterically occluded or inflexible S2 pockets. CypD by contrast contains a relatively un-occluded S2 pocket and flexible R124 residue. IC₅₀ values reflect mean ± s.e.m. of three technical replicates. Data points and error bars reflect mean ± s.d. of individual assays at one dose.

and **B25** than cyclophilins that retain lysine at this position (CypD, CypA, CypB, CypE; Fig. 3d). The importance of this interaction was further supported by assaying several prolyl-isomerase-active CypD K118 mutants (Supplementary Fig. 3c). CypD K118A and CypD K118E are less potently inhibited by **B23** and **B25** (**B23**, IC₅₀^{CypD(K118A)} = 0.07 μM, IC₅₀^{CypD(K118E)} = 0.18 μM; **B25**,

IC₅₀^{CypD(K118A)} = 0.019 μM, IC₅₀^{CypD(K118E)} = 0.06 μM) than wild-type CypD (**B23**, IC₅₀^{CypD} = 0.0078 μM; **B25**, IC₅₀^{CypD} = 0.003 μM), consistent with the role of a salt bridge with K118 in enhancing CypD potency and selectivity (Supplementary Fig. 13b,c).

These observations refined our model for **B23** binding. Given the proximal placement of the carboxylate of **B23** to S123

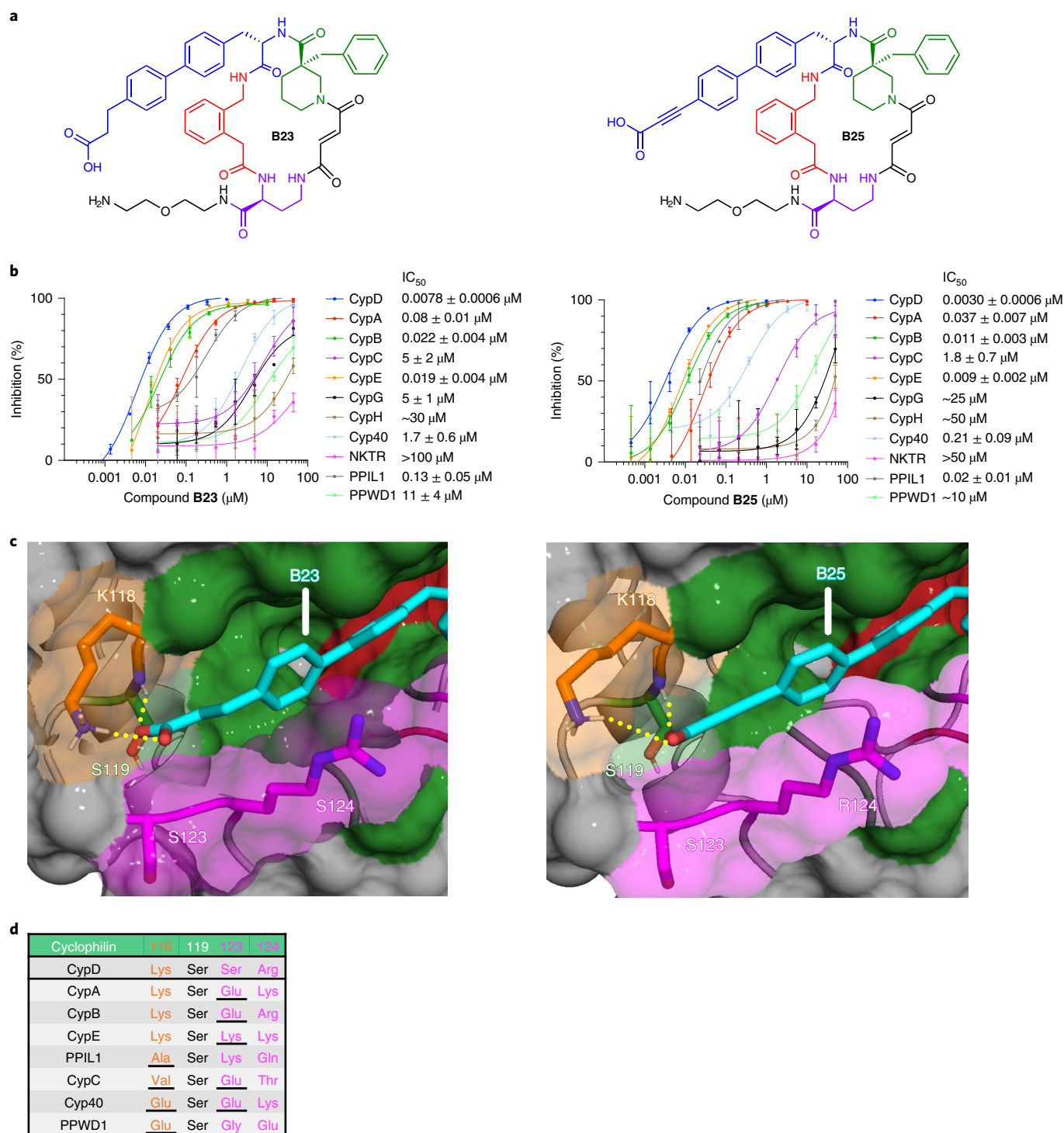


Fig. 3 | Carboxylate-containing biphenyl derivatives of B2 offer enhanced CypD selectivity. **a**, Structure of **B23** and **B25**. **b**, Cyclophilin prolyl-isomerase inhibition screens for **B23** and **B25**. **c**, Co-crystal structures of **B23** (PDB ID 7TH7, 1.18 Å resolution) and **B25** (PDB ID 7THC, 1.57 Å resolution) bound to CypD, viewing the S2 pocket. Active site binding is identical to that of **A26** (Fig. 1e). Yellow dashes indicate predicted hydrogen bonds. **d**, List of residues on the far side of the S2 pocket of cyclophilins that are proximal to the ligand carboxylates, with important deleterious interactions underlined. The biphenyl group with 3-carbon carboxylates, **B23** and **B25**, achieve strong selectivity over cyclophilins without a residue homologous to CypD K118. **B23** and **B25** show similar inhibition potencies for CypD and other cyclophilins that contain a Lys residue homologous to CypD K118, but slightly attenuated depending on the identity of residue 123. IC_{50} values reflect mean \pm s.e.m. of three technical replicates. Data points and error bars reflect mean \pm s.d. of individual assays at one dose.

and R124, these two residues may also contribute to the partial selectivity of **B23** for CypD. We therefore generated S123E, R124A, and R124K CypD mutants, which retain PPI activity

(Supplementary Fig. 3c), and assayed inhibition by **B23** and **B25**. **B23** and **B25** exhibit reduced potency against CypD S123E as compared to wild-type CypD (Supplementary Fig. 14b,c).

CypD S123E shares the exact same S2 pocket residues with CypB (Supplementary Fig. 14f), and for both proteins we observe a decrease in IC_{50} of threefold compared with wild-type CypD for **B23** and **B25** (**B23**, $IC_{50}^{CypB} = 0.022 \mu\text{M}$, $IC_{50}^{CypD(S123E)} = 0.023 \mu\text{M}$;

B25, $IC_{50}^{CypB} = 0.011 \mu\text{M}$, $IC_{50}^{CypD(S123E)} = 0.008 \mu\text{M}$). We reasoned that S123 can better tolerate the carboxylate on **B23** in comparison to a negatively charged Glu at this position in CypB. This hypothesis was further supported by the conformational difference in the S123 backbone loop between co-crystal structures of **B2** versus **B23** bound to CypD (Extended Data Fig. 4a,b). Migration of the S123 loop in the **B23**–CypD structure compared to **B2**–CypD suggests that this conformational shift must be tolerated for any cyclophilin bound to **B23** (Extended Data Fig. 4a,b). Indeed, other cyclophilins with Glu at the 123 position (CypA, CypB, CypC, Cyp40) show weaker inhibition by **B23** compared to CypD. Surprisingly, neither **B23** nor **B25** show any appreciable difference in potency for CypD R124A or R124K compared to wild-type CypD, suggesting that R124 plays a minimal role in **B23** or **B25** binding (Supplementary Fig. 15b,c). Collectively, these observations suggest that the S123 gatekeeper plays a role in the selectivity profile of **B23** and **B25**.

Using these co-crystal structures and mutational analyses, we sought to achieve improved CypD selectivity over cyclophilins that share K118 (CypA, CypB, CypE) by installing carboxylate groups predicted to be positioned closer to the non-conserved S123 in CypD. Several of the resulting inhibitors retain similar potencies to **B23**, but none offer improvements in selectivity (**B35**–**B39**; Supplementary Fig. 16a–e). Many deleterious modifications were observed, including functionalizing the ethylene linker of **B23**, or altering the position of the carboxylate on the biphenyl group (**B40**–**B50**; Supplementary Fig. 17a–k). These modifications presumably change the location and binding mode of the carboxylate with respect to K118 and S119, thereby decreasing potency with no selectivity benefit. We reasoned that to gain further CypD selectivity, we must maintain the carboxylate's interactions with K118 and S119 and add groups that can be presented to the S123 position. As the analogous S123 position is a more sterically bulky lysine in CypE, and a negatively charged glutamate in CypA and CypB, presenting a carboxylate group closer to this region could contribute additional CypD selectivity over these cyclophilins (Extended Data Fig. 1d,e). We subsequently made a disubstituted nitrile/carboxylate biphenyl derivative (**B51**), similar to **B34**, and two dicarboxylate moieties (**B52**, **B53**) to test this hypothesis.

While the nitrile of **B51** only hampers the selectivity compared to the **B23** carboxylate (Supplementary Fig. 18a), **B52** and **B53**, which contain malonate or glutarate moieties, respectively, retain CypD potency (**B52** $IC_{50}^{CypD} = 0.010 \mu\text{M}$; **B53** $IC_{50}^{CypD} = 0.057 \mu\text{M}$) compared to **B23**, while further improving CypD selectivity (Fig. 4a,b and Supplementary Fig. 18b,c). **B52** and **B53** show ~15- to 30-fold selectivity for inhibiting CypD over the most closely related cyclophilins, CypE and CypB, 60- to 900-fold selectivity over CypA and PP1L1, and >900-fold selectivity against the remaining six cyclophilins (Extended Data Fig. 5). The 100-fold selectivity of **B52** and **B53** for CypD over CypA is especially noteworthy since CypA is the most abundantly expressed cyclophilin in human cells, and one of the most abundantly expressed intracellular proteins (Supplementary Table 1). We then solved co-crystal structures of **B52** and **B53** bound to CypD (Fig. 4c; PDB IDs 7THD, 7THF). We observed a similar binding mode as **B23**, maintaining a salt bridge with K118, but now presenting a second carboxylate in the proximity of the S123 and R124 residues, as designed. For **B52**, we also observed a novel hydrogen bond with the backbone atoms between S123 and R124. We therefore attributed the selectivity of **B52** and **B53** for CypD over CypA, CypB, and CypE to the presentation of the second carboxylate near S123 (Fig. 4d).

To test this basis of selectivity, we assayed **B52** and **B53** against CypD gatekeeper mutants S123E, R124A, and R124K (Supplementary Figs 14d,e and 15d,e), along with K118A and

K118E mutants (Supplementary Fig. 13d,e). We observed similar trends as seen with monocarboxylates **B23** and **B25** compared with wild-type CypD—decreased potency for CypD S123E (**B52** $IC_{50}^{CypD(S123E)} = 0.24 \mu\text{M}$; **B53** $IC_{50}^{CypD(S123E)} = 0.8 \mu\text{M}$) roughly equal

to CypB (**B52** $IC_{50}^{CypB} = 0.21 \mu\text{M}$; **B53** $IC_{50}^{CypB} = 1.1 \mu\text{M}$), little to no ablation of potency for the CypD R124A and R124K mutants, and a decrease in potency for CypD K118A (**B52** $IC_{50}^{CypD(K118A)} = 0.073 \mu\text{M}$; **B53** $IC_{50}^{CypD(K118A)} = 0.9 \mu\text{M}$) and K118E (**B52** $IC_{50}^{CypD(K118E)} = 0.3 \mu\text{M}$; **B53** $IC_{50}^{CypD(K118E)} = 4 \mu\text{M}$) mutants upon removing the possibility of an inhibitor–protein salt bridge. These results suggest that **B52** and **B53** achieve substantial CypD selectivity on the basis of favorable contacts with its K118 and S123 residues, and on the absence of such interactions with homologous positions in other cyclophilins.

To further establish the dependence of CypD inhibitor potency on S2 pocket residues, we sought to rescue the attenuated potency of **B52** and **B53** for both CypB and CypA by installing gatekeeper mutations to match the residues of CypD in this pocket (CypB E121S, CypA E81S/K82R). Both CypB E121S and CypA E81S/K82R mutants retain prolyl-isomerase activity (Supplementary Fig. 3d,e). As expected, both **B52** and **B53** have similar potencies for CypD as CypB E121S (**B52**, $IC_{50}^{CypD} = 0.010 \mu\text{M}$, $IC_{50}^{CypB(E121S)} = 0.008 \mu\text{M}$; **B53**, $IC_{50}^{CypD} = 0.057 \mu\text{M}$, $IC_{50}^{CypB(E121S)} = 0.05 \mu\text{M}$), rescuing the 15- to 20-fold inhibition potency difference of **B52** and **B53** for CypD versus wild-type CypB (**B52**, $IC_{50}^{CypB} = 0.21 \mu\text{M}$; **B53**, $IC_{50}^{CypB} = 1.1 \mu\text{M}$)

(Extended Data Fig. 6a and Supplementary Fig. 19d,e). Similarly, we observed **B52** and **B53** to have similar potencies for CypD and CypA E81S/K82R (**B52**, $IC_{50}^{CypD} = 0.010 \mu\text{M}$, $IC_{50}^{CypA(E81S/K82R)} = 0.027 \mu\text{M}$; **B53**, $IC_{50}^{CypD} = 0.057 \mu\text{M}$, $IC_{50}^{CypA(E81S/K82R)} = 0.18 \mu\text{M}$), rescuing the ~100-fold inhibition potency difference of **B52** and **B53** for CypD versus wild-type CypA (**B52**, $IC_{50}^{CypA} = 1.1 \mu\text{M}$; **B53**, $IC_{50}^{CypA} = 3.4 \mu\text{M}$) (Extended Data Fig. 6b, Supplementary Fig. 20d,e). These trends were also conserved to a lesser degree for monocarboxylates **B23** and **B25** (Supplementary Figs 19b,c and 20b,c). Inhibition trends were maintained with fluorescein-labeled **A26** (**A26-FI**), **B52** (**B52-FI**), and **B53** (**B53-FI**), using a fluorescence polarization assay to measure binding against 11 prolyl-isomerase-active and five catalytically impaired or inactive cyclophilins (Extended Data Fig. 7a–c). While **A26-FI** promiscuously binds the 11 prolyl-isomerase-active cyclophilins, **B52-FI** and **B53-FI** exhibit selective CypD binding, corroborating prolyl-isomerase inhibition (Figs 1c and 4b). We also observed weak binding to the five impaired or non-PPIase active cyclophilins by **A26-FI**, **B52-FI**, and **B53-FI**, suggesting that their macrocycle scaffold cannot target these cyclophilins. Collectively, these results confirm that interactions between inhibitors and S2 pocket residues are strong determinants of CypD potency and selectivity.

We also reasoned that we could modify the S2 pocket of CypD to accommodate the amine containing compound **B32**, as it shows an alternate selectivity profile compared to most of our inhibitors, but has poor overall potency (Extended Data Fig. 6c,d and Supplementary Fig. 11b). We observed that replacing cationic residues within the S2 pocket of CypD (K118E, R124A) improves **B32** potency by 5- to 6-fold compared to wild-type CypD ($IC_{50}^{CypD} = 6 \mu\text{M}$, $IC_{50}^{CypD(K118E)} = 1.1 \mu\text{M}$, $IC_{50}^{CypD(R124A)} = 0.7 \mu\text{M}$; Extended Data Fig. 6c). Combining these two mutants (K118E/R124A) synergistically increases potency ($IC_{50}^{CypD(K118E/R124A)} = 0.06 \mu\text{M}$), a 100-fold improvement compared to wild-type CypD (Extended Data Fig. 6c). **B32** exhibits good selectivity for CypD K118E/R124A over wild-type cyclophilins, with at least 13-fold preference over the nearest cyclophilin, PPWD1 (Supplementary Fig. 11b) and >100-fold selectivity over CypA. Overall, **B32** and CypD K118E/

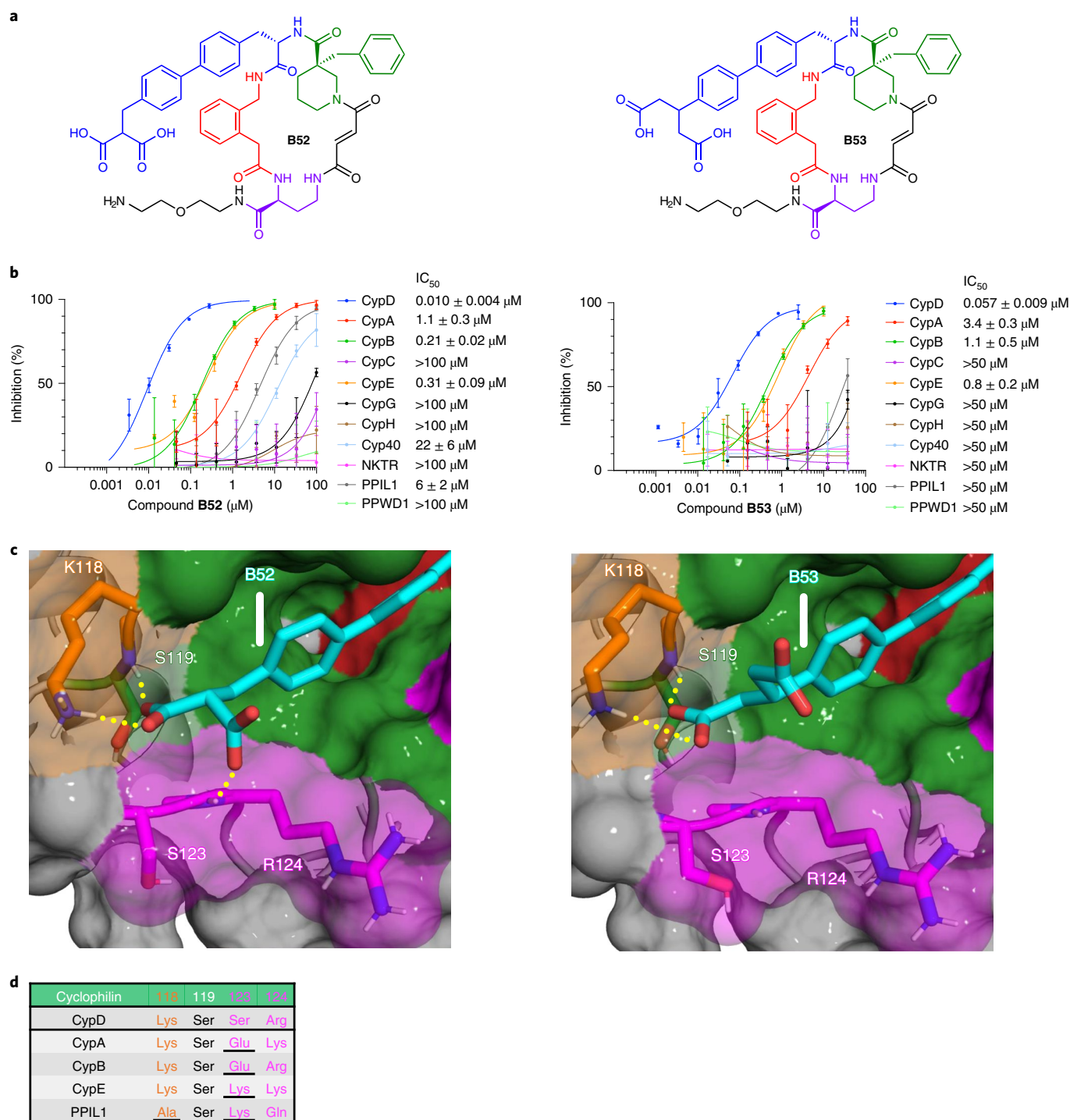


Fig. 4 | Biphenyl dicarboxylates achieve strong CypD selectivity. **a**, Structure of **B52** and **B53**. **b**, Cyclophilin prolyl-isomerase inhibition screens for **B52** and **B53**. **c**, Co-crystal structures of **B52** (PDB ID 7THD, 1.16 Å resolution) and **B53** (PDB ID 7THF, 1.10 Å resolution) bound to CypD, viewing the S2 pocket. Active site binding is identical to **A26** (Fig. 1e). Yellow dashes indicate predicted hydrogen bonds. **d**, List of residues on the far side of the S2 pocket of cyclophilins that are proximal to the ligand carboxylates. Both compounds retain CypD potency similar to that of mono-carboxylate **B23**, while enhancing selectivity over CypA, CypB, CypE, and PPIL1. The malonic and glutaric acids of **B52** and **B53**, respectively, position the carboxylate in a similar pose as **B23** (Fig. 3c), while presenting a second carboxylate to the S123 residue. **B52** forms a predicted hydrogen bond with the peptide backbone of S123–R124. R124 is pushed out of the S2 pocket, consistent with other macrocycles containing large S2-binding groups such as **B1**. **B52** and **B53** achieve selectivity over CypA and CypB through charge repulsion with a glutamate at the analogous 123 position, while creating a steric clash with PPIL1 and the lysine of CypE at this same position. IC_{50} values reflect mean \pm s.d. of four independent replicates (each comprising three technical replicates). Graphs show a representative single independent replicate (independent replicate 1 is shown, containing three technical replicates) with data points and error bars reflecting mean \pm s.d. of individual assays at one dose. Further independent replicates are shown in Supplementary Fig. 18b,c.

R124A provide another cyclophilin–ligand pair with selective inhibition dependent on S2 pocket identity.

CypD inhibitors are active in mitochondria. The lack of reliable functional CypD assays in intact cells makes it difficult to directly measure CypD inhibition in intact cell culture. Consistent with multiple previous reports, our efforts to use a calcein–Co²⁺ assay and mitochondrial membrane potential dyes in cells to characterize our compounds with CsA as a control failed to reliably assess mPTP opening in a CypD-inhibition-dependent manner and were also prone to confounding signals^{39–44}. For these reasons, CypD inhibitors have mostly been characterized biochemically *in vitro*, or in isolated mitochondria^{13,16,45–47}.

We tested the ability of our CypD-selective macrocycles to inhibit CypD in active mitochondria isolated from mouse liver. First, we verified that modifying groups on the ‘tail’ position of **B52** and **B53** (for example, **B52-A**, **B53-A**) do not affect potency or selectivity, and that their enantiomers do not inhibit any cyclophilin (***B52-A**, ***B53-A**) (Supplementary Fig. 21a–d). Since CypD is exclusively found in mitochondria, we appended Cy5, an established mitochondrial localization group⁴⁸, to all four macrocycles at the ‘tail’ position (**B52-Cy5**, **B53-Cy5**, ***B52-Cy5**, ***B53-Cy5**). We observed minimal change in potency or selectivity for CypD *in vitro* upon addition of the Cy5 group (Supplementary Fig. 22a–d). We then tested compounds **B52-Cy5** and **B53-Cy5** in isolated mouse liver mitochondria, measuring their calcium retention before a mPTP opening event. In comparison to the dimethylsulfoxide (DMSO) control, we observed substantially increased calcium retention capacity before mPTP opening when pretreated with CsA, **B52-Cy5**, or **B53-Cy5** (Fig. 5a–d and Supplementary Fig. 23a,b). Importantly, inactive enantiomers ***B52-Cy5** and ***B53-Cy5** do not inhibit CypD *in vitro* (Fig. 5a–d and Supplementary Fig. 23a,b) and do not influence calcium retention capacity before mPTP opening, strongly supporting CypD-dependent inhibition of mPTP opening by **B52-Cy5** and **B53-Cy5**.

As expected, while **B52-Cy5** and **B53-Cy5** engage CypD in isolated mitochondria, we did not observe efficient plasma membrane permeability of **B52-Cy5**, **B53-Cy5**, or their inactive enantiomers by fluorescence microscopy (Extended Data Fig. 8a–i and Supplementary Fig. 24b–f), presumably because of the presence of dicarboxylate groups. To improve cell permeability, we used a pro-drug strategy and prepared both sets of active and inactive enantiomers as ethyl esters (**B52-Et-Cy5**, **B53-Et-Cy5**, ***B52-Et-Cy5**, ***B53-Et-Cy5**) (Fig. 5e and Supplementary Fig. 24a). We observed strong mammalian cell permeability and mitochondrial localization for all four ester-containing compounds (Fig. 5f, Extended Data Fig. 8a–i and Supplementary Fig. 24b–f). These ester derivatives did not potently inhibit the prolyl-isomerase activity of CypD, consistent with the importance of the dicarboxylate groups (Supplementary Fig. 25). All four pro-drug compounds were hydrolyzed to their active dicarboxylate forms *in vitro* with human carboxylesterase (CES1), and **B52-Et-Cy5**, ***B52-Et-Cy5**, and **B53-Et-Cy5** were readily converted to the corresponding di-acids intracellularly by endogenous esterases in a variety of human (A549, HeLa, HEK293T, HepG2) and mouse (mouse embryonic fibroblasts (MEFs)) cell lines (Extended Data Fig. 9a–h).

These findings, coupled with robust CypD-dependent inhibition of mPTP opening in isolated mitochondria, suggest that pro-drug versions of Cy5-conjugated **B52** and **B53** can access mitochondria and release active CypD-selective inhibitors in mammalian cells. These observations make esterified **B52** and **B53** attractive candidates for potent and selective probes of CypD activity in biological systems.

Development of CypE-selective inhibitors. Since CypD-selective inhibitors **B52** and **B53** were designed from a slightly promiscuous inhibitor **B2**, we next explored the possibility of selectively

modulating a different cyclophilin by using covalent inhibition. While most covalent inhibitors target catalytic residues, the non-conserved residues in cyclophilin S2 pockets are both solvent-exposed and non-catalytic. Many cyclophilins contain non-catalytic lysines in their S2 pocket (Extended Data Fig. 1d,e). Although non-catalytic lysines are typically protonated at physiological pH, aryl boronic acid carbonyls have been shown to modify lysine and N-terminal groups covalently and reversibly through the formation of iminoboronates. Previous studies have incorporated aryl boronic acid carbonyl warheads on inhibitors to covalently modify non-catalytic lysines⁴⁹. We hypothesized that installing this reactive group on the biphenyl of inhibitor **B2** might allow a reversible covalent interaction with one of these cyclophilins, potentially providing a new subtype-selective inhibitor. We synthesized ketone (**C1A**, **C2A**) and aldehyde boronic acids (**C3A**, **C4A**) that could place this warhead close to cyclophilin S2 pocket lysine residues (Supplementary Fig. 26a–d).

We screened these four compounds in a fluorescence polarization competition assay with **A26-FI** against seven lysine-containing cyclophilins (Supplementary Fig. 26a–d), identifying **C3A** as a potent inhibitor of **A26-FI** binding to CypE (K_i of 0.072 μ M) (Fig. 6a,b and Supplementary Fig. 26c). Additionally, **C3A** showed ≥ 10 -fold selectivity for CypE over other tested cyclophilins. Shifting the aldehyde group to the meta position of the ring (**C4A**) attenuated CypE potency and selectivity, suggesting improper placement of **C4A**'s aryl boronic acid carbonyl towards the lysines of CypE (Supplementary Fig. 26d). Replacing the aldehyde with a ketone (**C1A**, **C2A**) also decreased potency for CypE compared to **C3A** (Supplementary Fig. 26a,b). Compounds **C5A** and **C6A** containing either the aldehyde or the boronic acid alone, respectively, showed reduced potency by 16-fold and 100-fold, respectively, relative to **C3A** (Supplementary Fig. 27a–c). Since the potency of **C3A** is contingent on both the boronic acid and the aldehyde, these results suggest **C3A** is acting covalently through iminoboronate formation with CypE, consistent with the lysine-rich S2 pocket of CypE (Extended Data Fig. 1d,e).

Macrocycle **C3A** is also a potent inhibitor against CypE prolyl-isomerase activity, with an IC_{50} of 0.013 μ M (Fig. 6c and Supplementary Fig. 28b). **C3A** is also very selective for CypE with an IC_{50} that is at least 30- to 4,000-fold more potent for CypE than the other ten cyclophilins screened. Once again, replacement of the aldehyde with a ketone (**C1A**, $IC_{50}^{CypE} = 0.9 \mu$ M), or removal of either the boronic acid (**C5A**, $IC_{50}^{CypE} = 1 \mu$ M) or the aldehyde (**C6A**, $IC_{50}^{CypE} = 4 \mu$ M) drastically reduces both the potency and selectivity compared to **C3A**, again supporting that **C3A** inhibits CypE covalently (Supplementary Fig. 28a–e).

Mass spectrometry did not detect a clear lysine-modified covalent adduct between **C3A** and CypE (Extended Data Fig. 10a). We speculated that reducing the iminoboronate intermediate with sodium cyanoborohydride (NaCNBH₃) might trap the covalent adduct. Indeed, co-incubating **C3A** in fivefold excess for 1 h with CypE followed by treatment with 25 mM NaCNBH₃ resulted in observation of a +806 Da adduct, corresponding to the reductive amination product minus water (Fig. 6d), but not for boronic acid **C6A** (Extended Data Fig. 10b). The loss of water has been reported for other aryl boronic acid carbonyl inhibitors treated with NaCNBH₃⁴⁹. These findings suggest that **C3A** functions in a reversible covalent manner. We also observed +779 Da covalent adduct formation under these conditions with aldehyde-only **C5A**, suggesting that carbonyl groups at this position can form imines with S2 pocket lysines of CypE (Extended Data Fig. 10b). Nonetheless, the 75-fold higher CypE inhibition potency of **C3A** over **C5A** suggests that this reversible interaction is substantially stronger for **C3A**. Little or no covalent modification for 12 other cyclophilins was observed when treated with **C3A** and NaCNBH₃, establishing the selectivity of this covalent interaction (Supplementary Fig. 29a,b).

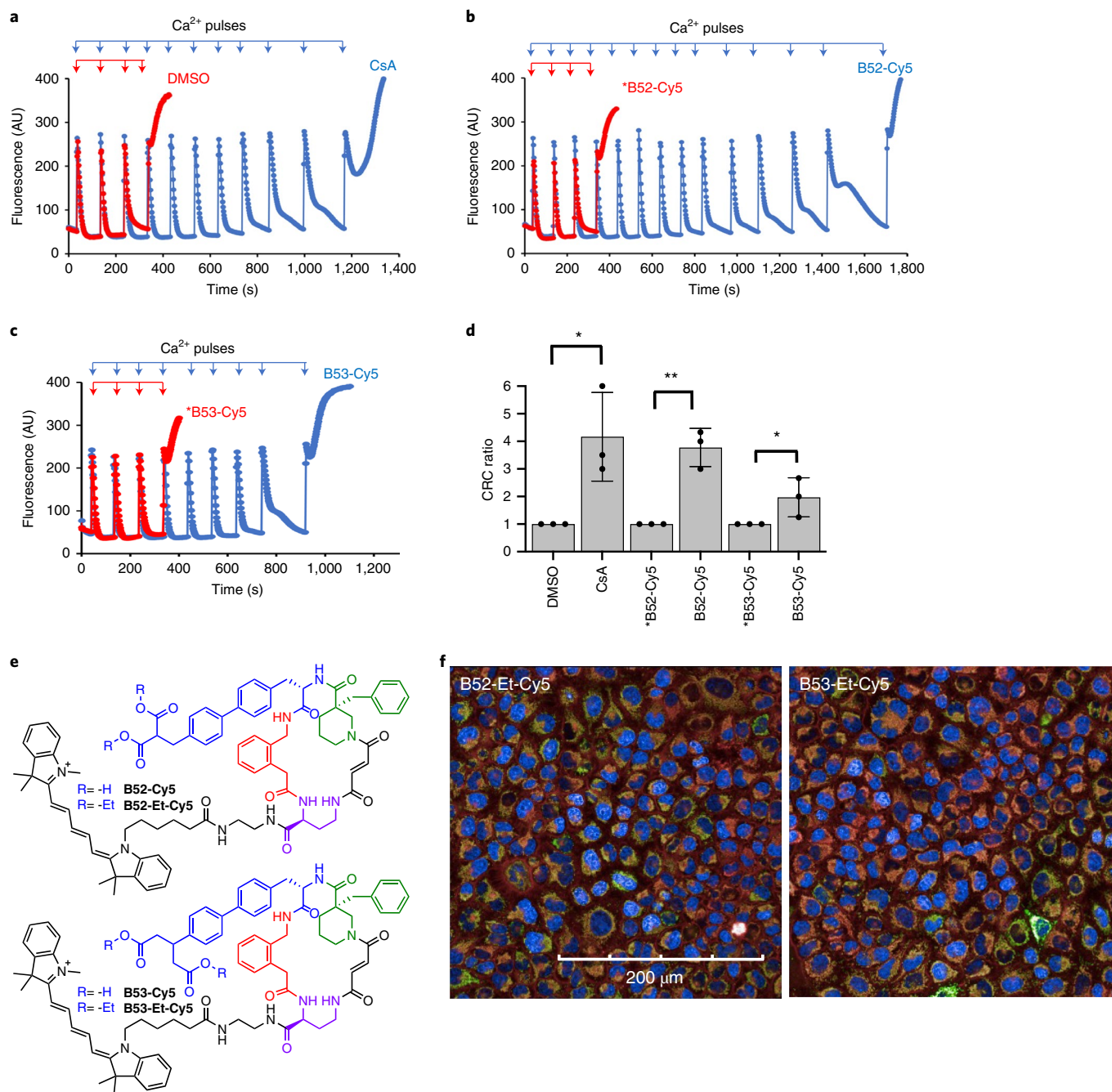


Fig. 5 | Cy5-conjugated cyclophilin D inhibitors delay calcium induced opening of the mPTP in isolated mouse liver mitochondria and enter human cells as ester prodrugs. The calcium retention capacity of mitochondria was determined in isolated mouse liver mitochondria ($0.5 \mu\text{g mL}^{-1}$) in response to pulses of $60 \mu\text{M}$ CaCl_2 in the presence of the indicated CypD inhibitors (or inactive enantiomers). Concentrations used were $2 \mu\text{M}$ CsA, $10 \mu\text{M}$ B52-Cy5, $10 \mu\text{M}$ *B52-Cy5, $20 \mu\text{M}$ B53-Cy5, $20 \mu\text{M}$ *B53-Cy5. Mitochondrial uptake of extramitochondrial Ca^{2+} was assessed by monitoring the fluorescence of Calcium green 5n, depicted in arbitrary units (AU). The rapid increase in fluorescence after several pulses of Ca^{2+} are taken up corresponds to mitochondrial Ca^{2+} release through mPTP opening. **a–c**, Traces are shown from a representative experiment, with all assays performed on the same mitochondrial preparation and day. **d**, Quantitation of calcium retention capacity (CRC) reported as the ratio of the number of Ca^{2+} pulses required to induce mPTP opening in the listed condition relative to DMSO control conditions on the same mitochondrial preparation and day. **e**, Structures of Cy5-conjugated CypD-selective inhibitors and prodrugs. **f**, Fluorescence microscopy of HeLa cells co-incubated with ester prodrugs B52-Et-Cy5 and B53-Et-Cy5 (red), co-stained with mitochondrial (green) and nuclear (blue) dyes (Mitotracker Green and Hoechst 33342, respectively). Both prodrugs show good plasma membrane permeability and co-localization with Mitotracker Green, quantified in Extended Data Fig. 8a–i. Calcium retention data are from three independent experiments/mitochondrial isolations. Data bars and error bars represent mean \pm s.d. DMSO versus CsA, $P=0.0135$; *B52-Cy5 versus B52-Cy5, $P=0.0011$; *B53-Cy5 versus B53-Cy5, $P=0.0382$. * $P < 0.05$, ** $P < 0.005$ by one-sided Student's *t*-test. Microscopy images are a representative image of three technical replicates. Scale bars, $200 \mu\text{m}$.

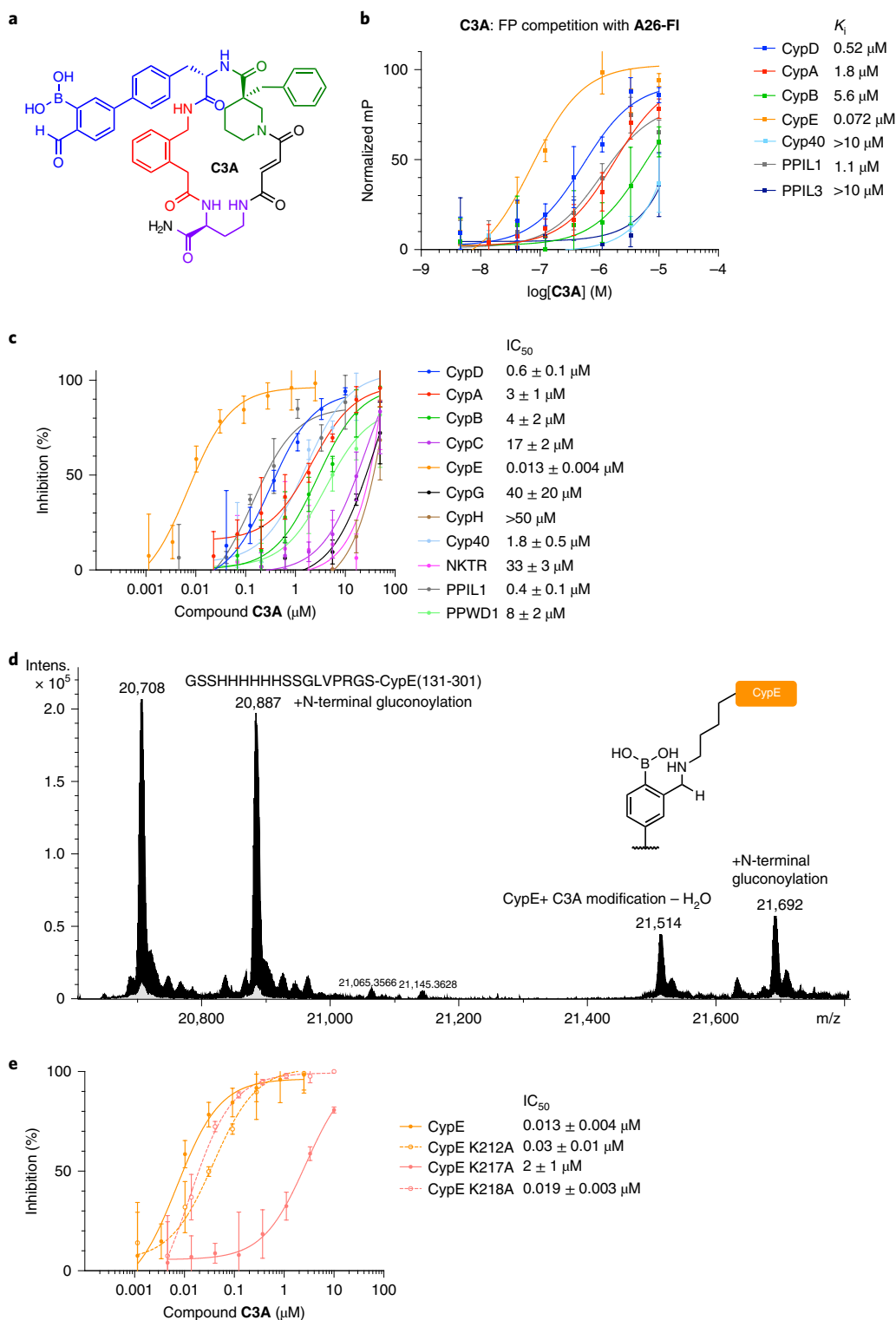


Fig. 6 | Aryl-carbonyl boronic acid C3A achieves selective inhibition of CypE. **a**, Structure of C3A. **b**, C3A fluorescence polarization (FP) competition with A26-FI against cyclophilins with S2 pocket lysines. **c**, Cyclophilin prolyl-isomerase inhibition screen of C3A, showing potency and selectivity for CypE. **d**, Mass spectrometry trace of CypE incubated with C3A and reduced with sodium cyanoborohydride. C3A shows an adduct consistent with CypE + amine-H₂O (+806 Da), the result of iminoboronate formation followed by reductive amination. The mass of CypE is 20,708 Da, The CypE preparation also included N-terminal gluconoylation. **e**, Prolyl-isomerase inhibition by C3A against CypE S2 pocket lysine to alanine mutants. For the FP assay, the y-axis is normalized to internal control wells containing A26-FI only (100%) and A26-FI with cyclophilin (0%). Values reflect mean of three technical replicates and error bars reflect s.d. of individual assays at one dose. For the prolyl-isomerase assay in **c** and the CypE wild-type dose-response curve in **e**, IC_{50} values reflect mean \pm s.d. of four independent replicates (each comprising three technical replicates). Graph shows a representative single independent replicate (Independent replicate 3 is shown, containing three technical replicates) with data points and error bars reflecting mean \pm s.d. of individual assays at one dose. Further independent replicates are shown in Supplementary Fig. 28b. For the prolyl-isomerase assay in **e**, IC_{50} values for the CypE mutants reflect mean \pm s.e.m. of three technical replicates, while data points and error bars reflect mean \pm s.d. of individual assays at one dose.

To determine which CypE lysine residue is covalently modified by **C3A**, we generated alanine point mutants at each of the three S2 pocket lysines of CypE (K212A, K217A, K218A). Binding and inhibition potency by **C3A** for CypE K212A and K218A mutants was similar to wild-type CypE (Fig. 6e and Supplementary Figs 30b and 31b). By contrast, **C3A** was 40-fold less potent at competing **A26-FI** from CypE K217A ($K_i^{\text{CypE}(K217A)} = 3.1 \mu\text{M}$) compared to wild-type CypE ($K_i^{\text{CypE}} = 0.072 \mu\text{M}$), and was 150-fold less potent at inhibiting K217A prolyl-isomerase activity ($\text{IC}_{50}^{\text{CypE}(K217A)} = 2 \mu\text{M}$) compared to wild-type CypE ($\text{IC}_{50}^{\text{CypE}} = 0.013 \mu\text{M}$).

Collectively, these results indicate that our model for achieving subtype-selective cyclophilin inhibition can be translated to other cyclophilin proteins, resulting in potent and selective CypE inhibition through reversible covalent bonding with the S2 pocket K217 residue of CypE.

Discussion

We tailored promiscuous initial ligands from a DNA-templated library that bind cyclophilin active sites through iterated cycles of structural studies, mutagenesis, and small-molecule engineering to generate what are, to our knowledge, the first reported potent and subtype-selective inhibitors of CypD and of CypE. Cyclophilin subtype selectivity emerged through carefully engineered engagement with poorly conserved residues in the S2 pocket, an exo-site adjacent to each cyclophilin's active site. Our results also suggest the feasibility of discovering subtype-selective cyclophilin ligands through parallel selections using a panel of subtypes to identify putative selective binders through their selective enrichment.

Structure–activity relationships and mutational analyses refined our model for CypD selectivity, which we applied to develop other selective cyclophilin inhibitors. CsA, an active-site-binding cyclophilin inhibitor, shows minimal selectivity for CypD over other cyclophilins and mutants (Extended Data Figs 1a–c and 5, Supplementary Table 2, and Supplementary Figs 13a, 14a, 15a, 19a, 20a and 31a). By contrast, our inhibitors that bind both the active site and S2 pocket of CypD offer improved selectivity (Extended Data Fig. 5 and Supplementary Table 2). The inclusion of large hydrophobic groups (**B1**, **B2**) into the S2 pocket eliminated off-target inhibition of CypG, CypH, and NKTR owing to the presence of inflexible or hydrophobic residues within their S2 pockets (Fig. 2a–d, Extended Data Fig. 5, and Supplementary Table 2). CypD, by contrast, contains a displaceable R124 residue that migrates upon ligand binding (Supplementary Figs 5a–c and 32).

Selectivity for CypD was further improved by installing carboxylates (**B23**, **B25**) that can hydrogen bond with S119 and K118, achieving selectivity over non-lysine-containing PPIL1, Cyp40, CypC, and PPWD1 (Fig. 3a–d, Extended Data Fig. 5, and Supplementary Table 2). To confer selectivity over K118-containing CypA, CypB, and CypE, we installed a second carboxylate (**B52**, **B53**) to interact with the gatekeeper residues on each cyclophilin, which show high potency and selectivity for CypD (Fig. 4a–d). CypD S123 can sterically and electronically tolerate dicarboxylates, while Glu at the analogous position in CypA and CypB presumably repels the dicarboxylate, and the more bulky lysine of CypE may sterically clash with the dicarboxylate (Fig. 4d, Extended Data Fig. 5, and Supplementary Table 2). Complementing these trends is the overall migration of S2 pocket residues in CypD to accommodate ligand binding (Extended Data Fig. 4b and Supplementary Fig. 32). Conformational flexibility of K118, S123, and R124 is dependent on the size and functionality of the binding ligand, as growing the S2-binding moiety of the ligand, while installing hydrogen-bond interactions, induces this residue migration (Supplementary Video 1).

Dicarboxylate groups on the inhibitors developed in this study thus provide a chemical environment that CypD, but not other

cyclophilins, can accommodate. This model was further supported with molecular footprinting analysis of JOMBt compared to **B52** (Supplementary Fig. 33). JOMBt is reliant on weak binding energy per residue on highly conserved cyclophilin active site residues, while **B52** owes its potent CypD binding to unique S2 pocket residues that are poorly conserved between other family members. The conformational flexibility of K118, S123 and R124 is consistent with previous reports¹ that suggest the S2 pocket of each cyclophilin may confer endogenous substrate-binding selectivity, whereby prolyl isomerization of a peptide substrate at the active site is only accessible if the S2 pocket can tolerate upstream amino acids. Indeed, the S2 pockets of each cyclophilin vary in their tolerance of different groups in our inhibitors. This observation is consistent with the S2 exo-site serving as a substrate-binding pocket separate from the active site that confers substrate selectivity. We further established that S2 pocket interactions are the basis of observed subtype selectivity through rational mutagenesis of the S2 pocket of CypD to accommodate a positively charged amine-containing ligand **B32** (Extended Data Fig. 6c,d and Supplementary Table 2).

We further extended these insights to achieve selective CypE inhibition. **C3A** selectively targets CypE through reversible covalent bonding with its S2 pocket K217 residue (Fig. 6a–e). To our knowledge, **C3A** represents the first CypE-selective inhibitor and the second type of subtype-selective cyclophilin inhibitor after **B52** and **B53** (Supplementary Table 2). The aryl aldehyde boronic acid forms a reversible covalent bond with the K217 residue of CypE, while the presence of the boronic acid minimizes binding to the other cyclophilins. CypE is one of many cyclophilin proteins reported as a structural component of the spliceosome, but the assessment of its mechanistic role has been hampered by the lack of a cyclophilin-selective inhibitor²⁶. The use of CypE-selective inhibitors such as **C3A** may serve to illuminate the role of CypE in the spliceosome without confounding inhibition of the seven other spliceosome-associated cyclophilins²⁶.

The CypD-selective inhibitors developed in this work increase calcium retention capacity and delay mPTP opening in isolated mitochondria (Fig. 5a–d and Supplementary Fig. 23a,b). Ester pro-drug derivatives of these CypD-selective inhibitors also exhibit strong plasma membrane permeability, mitochondrial localization, and the ability to release active inhibitor in mammalian cells (Fig. 5e,f, Supplementary Figs 24a–f and 25, and Extended Data Figs. 8a–i and 9a–h). These compounds may serve as tools to explore the mechanism of action of the mPTP or as probes of the role of CypD in disease models with mPTP-oxidative stress as a phenotype, such as neurodegenerative disorders, IRI, liver diseases, and mitochondrial disorders.

More broadly, this study establishes that subtype-selective cyclophilin inhibition can be achieved through the design of ligands that interact with unique residues in cyclophilin exo-site S2 pockets (Extended Data Fig. 1d,e and Supplementary Table 2). Applying this strategy to develop additional selective cyclophilin inhibitors may unlock the biological or therapeutic potential of this family of targets, which have been relatively unexplored compared to others such as kinases, phosphatases, and proteases.

Online content

Any methods, additional references, Nature Research reporting summaries, source data, extended data, supplementary information, acknowledgements, peer review information; details of author contributions and competing interests; and statements of data and code availability are available at <https://doi.org/10.1038/s41589-022-01116-1>.

Received: 19 January 2022; Accepted: 19 July 2022;
Published online: 26 September 2022

References

- Davis, T. L. et al. Structural and biochemical characterization of the human cyclophilin family of peptidyl-prolyl isomerases. *PLoS Biol.* **8**, e1000439 (2010).
- Chen, J. et al. Biochemical features of recombinant human cyclophilin J. *Anticancer Res.* **36**, 1175–1180 (2016).
- Dunyak, B. M. & Gestwicki, J. E. Peptidyl-proline isomerases (PPIases): targets for natural products and natural product-inspired compounds. *J. Med. Chem.* **59**, 9622–9644 (2016).
- Austin, C. et al. *Prolyl Isomerases—Old Proteins as New Therapeutic Targets* (Selcia Ltd, 2015).
- Izzo, V., Bravo-San Pedro, J. M., Sica, V., Kroemer, G. & Galluzzi, L. Mitochondrial permeability transition: new findings and persisting uncertainties. *Trends Cell Biol.* **26**, 655–667 (2016).
- Briston, T., Selwood, D. L., Szabadkai, G. & Duchen, M. R. Mitochondrial permeability transition: a molecular lesion with multiple drug targets. *Trends Pharmacol. Sci.* **40**, 50–70 (2018).
- Baines, C. P. et al. Loss of cyclophilin D reveals a critical role for mitochondrial permeability transition in cell death. *Nature* **434**, 658 (2005).
- Nakagawa, T. et al. Cyclophilin D-dependent mitochondrial permeability transition regulates some necrotic but not apoptotic cell death. *Nature* **434**, 652–658 (2005).
- Mishra, J. et al. Cyclosporin A increases mitochondrial buffering of calcium: an additional mechanism in delaying mitochondrial permeability transition pore opening. *Cells* **8**, 1052 (2019).
- Kroemer, G., Galluzzi, L. & Brenner, C. Mitochondrial membrane permeabilization in cell death. *Physiol. Rev.* **87**, 99–163 (2007).
- Morciano, G. et al. Molecular identity of the mitochondrial permeability transition pore and its role in ischemia-reperfusion injury. *J. Mol. Cell. Cardiol.* **78**, 142–153 (2015).
- Martin, L. J. et al. GNX-4728, a novel small molecule drug inhibitor of mitochondrial permeability transition, is therapeutic in a mouse model of amyotrophic lateral sclerosis. *Front. Cell. Neurosci.* **8**, 1–7 (2014).
- Valasani, K. R. et al. Identification of a small molecule Cyclophilin D inhibitor for rescuing A β -mediated mitochondrial dysfunction. *ACS Med. Chem. Lett.* **7**, 294–299 (2016).
- Quintanilla, R. A., Jin, Y. N., Bernhardt, R., Von & Johnson, G. V. W. Mitochondrial permeability transition pore induces mitochondria injury in Huntington disease. *Mol. Neurodegener.* **8**, 1–19 (2013).
- Rao, V. K., Carlson, E. A. & Yan, S. S. Mitochondrial permeability transition pore is a potential drug target for neurodegeneration. *Biochim. Biophys. Acta Mol. Basis Dis.* **1842**, 1267–1272 (2018).
- Warne, J. et al. Selective inhibition of the mitochondrial permeability transition pore protects against neurodegeneration in experimental multiple sclerosis. *J. Biol. Chem.* **291**, 4356–4373 (2016).
- López-Erauskin, J., Ferrer, I., Galea, E. & Pujol, A. Cyclophilin D as a potential target for antioxidants in neurodegeneration: the X-ALD case. *Biol. Chem.* **394**, 621–629 (2013).
- Rasheed, M. Z., Tabassum, H. & Parvez, S. Mitochondrial permeability transition pore: a promising target for the treatment of Parkinson's disease. *Protoplasma* **254**, 33–42 (2017).
- Simón Serrano, S. et al. Evaluation of NV556, a novel cyclophilin inhibitor, as a potential antifibrotic compound for liver fibrosis. *Cells* **8**, 1409 (2019).
- Panel, M., Ghaleh, B. & Morin, D. Mitochondria and aging: a role for the mitochondrial transition pore? *Aging Cell* **17**, 1–15 (2018).
- Zhou, B. et al. Mitochondrial permeability uncouples elevated autophagy and lifespan extension. *Cell* **177**, 1–16 (2019).
- Taddeo, E. P. et al. Mitochondrial proton leak regulated by Cyclophilin D elevates insulin secretion in islets at nonstimulatory glucose levels. *Diabetes* **69**, 131–145 (2020).
- Carraro, M., Carrer, A., Urbani, A. & Bernardi, P. Molecular nature and regulation of the mitochondrial permeability transition pore(s), drug target(s) in cardioprotection. *J. Mol. Cell. Cardiol.* **144**, 76–86 (2020).
- Bround, M. J., Bers, D. M. & Molkentin, J. D. A 20/20 view of ANT function in mitochondrial biology and necrotic cell death. *J. Mol. Cell. Cardiol.* **144**, PA3–A13 (2020).
- Carraro, M., Checchetto, V., Szabó, I. & Bernardi, P. F-ATP synthase and the permeability transition pore: fewer doubts, more certainties. *FEBS Lett.* **593**, 1542–1553 (2019).
- Thapar, R. Roles of prolyl isomerases in RNA-mediated gene expression. *Biomolecules* **5**, 974–999 (2015).
- Theuerkorn, M., Fischer, G. & Schiene-Fischer, C. Prolyl *cis/trans* isomerase signalling pathways in cancer. *Curr. Opin. Pharmacol.* **11**, 281–287 (2011).
- Schiene-Fischer, C. Multidomain peptidyl prolyl *cis/trans* isomerases. *Biochim. Biophys. Acta Gen. Subj.* **1850**, 2005–2016 (2015).
- Frausto, S. D., Lee, E. & Tang, H. Cyclophilins as modulators of viral replication. *Viruses* **5**, 1684–1701 (2013).
- Kajitani, K. et al. Crystal structure of human cyclophilin D in complex with its inhibitor, cyclosporin A at 0.96-Å resolution. *Proteins* **70**, 1635–1639 (2007).
- De Simone, A. et al. A computationally designed binding mode flip leads to a novel class of potent tri-vector cyclophilin inhibitors. *Chem Sci.* **10**, 542–547 (2019).
- Ahmed-Belkacem, A. et al. Fragment-based discovery of a new family of non-peptidic small-molecule cyclophilin inhibitors with potent antiviral activities. *Nat. Commun.* **7**, 12777 (2016).
- Elkamhawy, A. et al. Novel quinazoline-urea analogues as modulators for A β -induced mitochondrial dysfunction: design, synthesis, and molecular docking study. *Eur. J. Med. Chem.* **84**, 466–475 (2014).
- Park, I. et al. Discovery of non-peptidic small molecule inhibitors of cyclophilin D as neuroprotective agents in A β -induced mitochondrial dysfunction. *J. Comput. Aided Mol. Des.* **31**, 929–941 (2017).
- Grädler, U. et al. Discovery of novel cyclophilin D inhibitors starting from three dimensional fragments with millimolar potencies. *Bioorg. Med. Chem. Lett.* **29**, 126717 (2019).
- Steadman, V. A. et al. Discovery of potent cyclophilin inhibitors based on the structural simplification of sanglifehrin A. *J. Med. Chem.* **60**, 1000–1017 (2017).
- Daum, S. et al. Isoform-specific inhibition of cyclophilins. *Biochemistry* **48**, 6268–6277 (2009).
- Usanov, D. L., Chan, A. I., Maiani, J. P. & Liu, D. R. Second-generation DNA-templated macrocycle libraries for the discovery of bioactive small molecules. *Nat. Chem.* **10**, 704–714 (2018).
- Legrand, O., Simonin, G., Perrot, J. Y., Zittoun, R. & Marie, J. P. Pgp and MRP activities using calcein-AM are prognostic factors in adult acute myeloid leukemia patients. *Blood* **91**, 4480–4488 (1998).
- Treulen, F., Uribe, P., Boguen, R. & Villegas, J. V. Mitochondrial permeability transition increases reactive oxygen species production and induces DNA fragmentation in human spermatozoa. *Hum. Reprod.* **30**, 767–776 (2015).
- Panel, M., Ghaleh, B. & Morin, D. Ca²⁺ ionophores are not suitable for inducing mPTP opening in murine isolated adult cardiac myocytes. *Sci. Rep.* **7**, 1–11 (2017).
- Chen, M. X. et al. Probing mitochondrial permeability transition pore activity in nucleated cells and platelets by high-throughput screening assays suggests involvement of protein phosphatase 2B in mitochondrial dynamics. *Assay. Drug Dev. Technol.* **16**, 445–455 (2018).
- Bhosale, G. & Duchen, M. R. Investigating the mitochondrial permeability transition pore in disease phenotypes and drug screening. *Curr. Protoc. Pharmacol.* **85**, e59 (2019).
- Connolly, N. M. C. et al. Guidelines on experimental methods to assess mitochondrial dysfunction in cellular models of neurodegenerative diseases. *Cell Death Differ.* **25**, 542–572 (2018).
- Schinzel, A. C. et al. Cyclophilin D is a component of mitochondrial permeability transition and mediates neuronal cell death after focal cerebral ischemia. *Proc. Natl Acad. Sci. USA* **102**, 12005–12010 (2005).
- Guo, H. X. et al. Novel cyclophilin D inhibitors derived from quinoxaline exhibit highly inhibitory activity against rat mitochondrial swelling and Ca²⁺ uptake/release. *Acta Pharmacol. Sin.* **26**, 1201–1211 (2005).
- Clarke, S. J., McStay, G. P. & Halestrap, A. P. Sanglifehrin A acts as a potent inhibitor of the mitochondrial permeability transition and reperfusion injury of the heart by binding to cyclophilin-D at a different site from cyclosporin A. *J. Biol. Chem.* **277**, 34793–34799 (2002).
- Zhou, L. et al. Mitochondria-localized self-reporting small-molecule-decorated theranostic agents for cancer-organelle transporting and imaging. *ACS Appl. Bio Mater.* **2**, 5164–5173 (2019).
- Akçay, G. et al. Inhibition of Mcl-1 through covalent modification of a noncatalytic lysine side chain. *Nat. Chem. Biol.* **12**, 931–936 (2016).

Publisher's note Springer Nature remains neutral with regard to jurisdictional claims in published maps and institutional affiliations.



Open Access This article is licensed under a Creative Commons Attribution 4.0 International License, which permits use, sharing, adaptation, distribution and reproduction in any medium or format, as long as you give appropriate credit to the original author(s) and the source, provide a link to the Creative Commons license, and indicate if changes were made. The images or other third party material in this article are included in the article's Creative Commons license, unless indicated otherwise in a credit line to the material. If material is not included in the article's Creative Commons license and your intended use is not permitted by statutory regulation or exceeds the permitted use, you will need to obtain permission directly from the copyright holder. To view a copy of this license, visit <http://creativecommons.org/licenses/by/4.0/>.

© The Author(s) 2022

Methods

General. Fmoc-protected amino acids and peptide coupling reagents were purchased from Chem-Impex International. Boronic acids or aryl halides were purchased from Combi-Blocks and Enamine, verified >95% pure by the manufacturer's standards. All other chemical reagents (verified >95% pure by manufacturer), PPIL4 (full length), and PPIL6(C-Myc/DDK), were purchased from Millipore-Sigma. SDCCAG-10(GST) was purchased from Abnova. Human recombinant CES1 and CES2 were purchased from R&D Systems. All purchased proteins were verified >85% pure by the manufacturer using SDS-PAGE. Nuclear magnetic resonance (NMR) spectra were gathered using a Bruker Ascend 400 MHz NMR. Quantification of DNA was completed using a NanoDrop One Microvolume UV-Vis Spectrophotometers (ThermoFisher Scientific). Preparative high-performance liquid chromatography (HPLC) reverse phase purification was conducted with an Agilent 6100 Quadrupole liquid chromatography–mass spectrometry (LC–MS) system using a Kinetex 5 μm C18 100 Å, AXIA Packed LC Column 150 \times 3.0 mm (Phenomenex). Silica gel column chromatography was conducted with a Biotage SP1 Flash Chromatography system. Recombinantly expressed proteins were purified using an AKTA pure fast protein liquid chromatography (FPLC). Quantitative PCR analysis was conducted using a CFX96 Touch Deep Well Real-Time PCR System (Bio-Rad). $^1\text{H-NMR}$ spectra for all reported compounds are provided in Supplementary Note 2 of the Supplementary Information. HRMS data is provided in Supplementary Tables 7 and 8. HPLC purity analysis of important compounds is included within Supplementary Note 2 of the Supplementary Information. All tested compounds were quantified with CH_2Cl_2 internal standard by $^1\text{H-NMR}$.

General mammalian cell culture conditions. HEK293T (American Type Culture Collection (ATCC) CRL-3216), HeLa (ATCC CCL-2), MEFs (ATCC CRL-2991), HepG2 (ATCC HB-8065), and A549 (ATCC CCL-185) cells were purchased from ATCC and cultured and passaged in Dulbecco's modified Eagle's medium (DMEM) plus GlutaMAX (ThermoFisher Scientific) for HEK293T/HeLa/MEFs, minimum essential medium (MEM; Corning) for HepG2, and F-12K (ATCC) for A549, each supplemented with 10% (v/v) fetal bovine serum (FBS; Gibco, qualified). All cell types were incubated, maintained, and cultured at 37 °C with 5% CO_2 . Cell lines were authenticated by their respective suppliers and tested negative for mycoplasma.

HPLC purity analyses of key compounds. Analytical analyses for compound purity was performed using an Agilent 6100 Quadrupole LC–MS system with a Kinetex 5 μm C18 100 Å LC Column 150 \times 2.1 mm (Phenomenex). Five microliters of 0.5–1 mM compound in DMSO- d_6 was injected and run for 3 min at 10% water/acetonitrile with 0.1% trifluoroacetic acid to elute off DMSO- d_6 . From 3 min to 15 min, gradient was increased to 100% acetonitrile, and held for 2 more min. Compound peaks were identified using the mass spectrometry trace. Purity analyses was quantified by percentage area of the compound peak at 214 nm absorbance relative to all identified peaks within the 3–17 min analysis window (to exclude the DMSO peak at 1.5 min).

Generation of His₆-Cyp expression constructs. Geneblock sequences for PPIF (UniProtKB Entry P30405: residues 45–207), PPIA (UniProtKB Entry P62937: residues 1–165), PPIB (UniProtKB Entry P23284: residues 34–216), PPID (UniProtKB Entry Q08752: residues 1–183), PPIH (UniProtKB Entry O43447: residues 1–177), PPIL1 (UniProtKB Entry Q9Y3C6: residues 1–166), and PPIL3 (UniProtKB Entry Q9H2H8: residues 1–161) were purchased from IDT and cloned into 2BT (UC Berkeley QB3 MacroLab) using ligation independent cloning. Gatekeeper mutations for PPIA and PPIB were introduced using site-directed mutagenesis with Q5 DNA polymerase (NEB) and primers from IDT. All constructs were verified using Sanger sequencing. *Escherichia coli* containing the constructs were cultured overnight at 37 °C in 2 \times YT medium (31 g in 1 L) containing 100 $\mu\text{g mL}^{-1}$ ampicillin.

PPIL2 (UniProtKB Entry Q13356: residues 280–457) cloned into pET28a LIC (Addgene Plasmid #25601), PPIG (UniProtKB Entry Q13427: residues 1–179) cloned into pET28a LIC (Addgene Plasmid #25137), PPIE (UniProtKB Entry Q9UNP9: residues 131–301) cloned into pET28a LIC (Addgene Plasmid #25605), PPWD1 (UniProtKB Entry Q96BP3: residues 473–646) cloned into pET28a LIC (Addgene Plasmid #25600), PPIC (UniProtKB Entry P45877: residues 24–212) cloned into pET28a LIC (Addgene Plasmid #25606), and NKTR (UniProtKB Entry P30414: residues 7–179) cloned into pET28a LIC (Addgene Plasmid #25597) were purchased as bacterial agar stabs and expressed in BL21DE3 cells. *E. coli* containing the constructs were cultured overnight at 37 °C in 2 \times YT medium (31 g in 1 L) containing 50 $\mu\text{g mL}^{-1}$ kanamycin.

Site-directed mutagenesis of CypD. Mutant CypD constructs were generated with primers for one-piece uracil-specific excision reactions (USER) containing a mutant overhang by PCR amplification of starting plasmids (Supplementary Table 3). PCR product was purified on microcentrifuge membrane columns (MinElute, Qiagen) and quantified by Nanodrop. Fragment (0.2 pmol, 7.5 μL) was combined in a 10 μL reaction mixture containing 0.75 μL (15 U) DpnI (NEB), 0.75 μL USER mix (endonuclease VIII and uracil-DNA glycosylase, NEB), 1 μL 10 \times CutSmart Buffer (NEB). Reactions were incubated at 37 °C for 30 min followed

by heating to 80 °C for 3 min and slow cooling to 12 °C at 0.1 °C s $^{-1}$. Constructs were directly transformed into One Shot Mach1 T1 Phage-Resistant Chemically Competent *E. coli* (Invitrogen) by heat shock for 30 s and streaked on 100 $\mu\text{g mL}^{-1}$ carbenicillin containing LB agar. Selected colonies with correct construct were verified by Sanger sequencing and cultured overnight in 2 \times YT supplemented with 100 $\mu\text{g mL}^{-1}$ carbenicillin. Plasmid was extracted by microcentrifuge membrane columns (QIAprep Spin Miniprep Kit, Qiagen) as per manufacturer's instructions and quantified by Nanodrop.

Site-directed mutagenesis of CypA, CypB, CypD (only for K175I mutant), and CypE. The K175I mutation for reduction of surface entropy⁵⁰ was introduced into the PPIF (CypD) construct and the gatekeeper residue mutations were introduced into the PPIA (CypA), PPIB (CypB), and PPIE (CypE) constructs via Quikchange site-directed mutagenesis (Agilent Technologies). Primers for the respective mutations are included in Supplementary Table 4. The template plasmid (~100 ng, 1 μL) was combined in a 25 μL mixture with forward and reverse primers (125 ng, 1.25 μL each), Q5 High-Fidelity DNA Polymerase (NEB) (1 μL , 2000 U mL $^{-1}$), deoxynucleoside triphosphate (dNTP) mix (10 mM, 1 μL), Q5 Reaction Buffer (NEB) (5 \times , 5 μL), and deionized H₂O (14 μL). Reactions were incubated at 98 °C for 120 s, followed by 30 cycles of 98 °C (10 s, melting), 55–60 °C (30 s, annealing), and 72 °C (5 min, elongation), followed by a final elongation cycle of 7 min. PCR products were transformed into *E. coli* DH5 α competent cells with a heat shock at 42 °C for 45 s and streaked onto Luria Broth agar plates containing 100 $\mu\text{g mL}^{-1}$ ampicillin (2BT) or 50 $\mu\text{g mL}^{-1}$ kanamycin (pET28 α LIC). Single colonies were isolated for inoculation and plasmid extraction via microcentrifuge membrane columns (QIAprep Spin Miniprep Kit, Qiagen), and mutations were verified by Sanger sequencing.

Recombinant expression and isolation of CypD and CypD mutants. CypD proteins were obtained from expression plasmids (Supplementary Table 5) by transforming into One Shot BL21(DE3) chemically competent *E. coli* (Invitrogen) by heat shock at 42 °C for 30 s. Cells were streaked onto agar plates containing 100 $\mu\text{g mL}^{-1}$ carbenicillin and incubated at 37 °C for 16 h. Individual colonies were grown up in a 2-L culture of LB medium supplemented with 100 $\mu\text{g mL}^{-1}$ carbenicillin at 37 °C until optical density reached 0.8. The culture was then cooled to 16 °C for 1 h and protein production was induced by adding 2 mL of 1 M isopropyl β -D-1-thiogalactopyranoside and left to incubate for 16 h. Cells were pelleted at 4,000g for 5 min at 4 °C and resuspended in 50 mL cold Tris-HCl pH 8.0, 50 mM NaCl, 5% glycerol (NiA Low Salt). Two Pierce protease inhibitor tablets (ThermoFisher Scientific) was added to the suspension and cells were subsequently lysed using an Avestin Emulsiflex-C3 homogenizer at 17,000–20,000 p.s.i. Lysed cells were pelleted, and supernatant was purified by FPLC affinity chromatography using a HisTrap HP 5 mL (GE) and a gradient of 0–100% NiA low salt/NiB low salt (NiB low salt: NiA low salt + 500 mM imidazole). Protein eluted off around 60–70%, confirmed by SDS-PAGE analysis of fractions. Isolated fractions were additionally purified by FPLC cation exchange, using a HiTrap SP 5 mL column (GE) and a gradient of 0–100% SA buffer/SB buffer (SA buffer: Tris-HCl pH 7.0, 1 mM dithiothreitol (DTT), 5% glycerol; SB buffer: SA buffer + 1 M NaCl). Fractions corresponding to >90% pure CypD came off around 40%, confirmed by SDS-PAGE. Combined fractions were dialyzed in 20 mM Tris-HCl pH 8.0, 50 mM NaCl, 1 mM DTT, 5% glycerol, using a Slid-A-Lyzer molecular weight cutoff = 3,000 dialysis cassette according to the manufacturer's instructions, overnight at 4 °C. Protein purity was >90% on the basis of SDS-PAGE gel electrophoresis and Coomassie staining. Pooled fractions were concentrated, flash frozen in liquid nitrogen, and stored at –80 °C. Protein was quantified using Pierce BCA Protein Assay Kit.

Recombinant expression and purification of CypA, CypB, CypC, CypE, CypG, CypH, Cyp40, NKTR, PPIL1, PPIL2, PPIL3, PPWD1. The expression plasmids for wild-type and mutant protein constructs (Supplementary Table 5) were transformed into *E. coli* BL21(DE3) competent cells with heat shock at 42 °C for 45 s. Cells were streaked onto Luria Broth agar plates containing 100 $\mu\text{g mL}^{-1}$ ampicillin (2BT) or 50 $\mu\text{g mL}^{-1}$ kanamycin (pET28 α LIC) and incubated overnight at 37 °C. Single colonies were inoculated into 2 \times YT medium supplemented with 1% glucose, 1 mM Mg²⁺, and 100 $\mu\text{g mL}^{-1}$ ampicillin (2BT) or 50 $\mu\text{g mL}^{-1}$ kanamycin (pET28 α LIC) and shaken at 37 °C until reaching an OD₆₀₀ = ~0.6–0.8. The cultures were then cooled to 16 °C for 1 h, and protein production was induced with 1 mM isopropyl β -D-1-thiogalactopyranoside overnight for 16–18 h. Cells were pelleted at 4,000g for 10 min at 4 °C before being homogenized in an Avestin Emulsiflex-C3 High Pressure Homogenizer at 17,000–20,000 p.s.i. three times and resuspended in buffer containing 20 mM Tris pH 8.0, 50 mM NaCl, and 5% glycerol. Lysates were centrifuged for 1 h at 17,000 r.p.m. at 4 °C in a Sorvall SLC6000 Fixed-Angle Rotor. Protein was purified from the supernatant via nickel affinity chromatography followed by cation exchange chromatography and size exclusion chromatography. First, the recombinant His₆-tagged proteins were purified with Ni(II)-affinity chromatography (HisTrap FF, GE Healthcare). The supernatant was run over the column, which was subsequently washed twice with buffer to remove non-specific binding. Two-milliliter fractions were eluted over 12 column volumes by increasing the imidazole concentration to 500 mM. For

PPIL2 and PPIL3, the His₆-tag was cleaved with TEV (2BT) or thrombin (pET28α LIC) overnight in pH 8.0 dialysis buffer containing 20 mM Tris base, 100 mM NaCl, 5 mM BME, 5% glycerol with a 3 kDa molecular weight cutoff filter. Proteins both with or without His-tag were diluted to reduce NaCl concentration in pH 8.0 buffer containing 20 mM Tris, 1 mM DTT, and 5% glycerol and loaded onto a cation exchange column (HiTrap SP, GE Healthcare). The column was washed with six column volumes of buffer to remove non-specific binding. Two-milliliter fractions were eluted over 12 column volumes with increasing salt gradient up to 1 M NaCl. Pooled fractions containing protein were concentrated and loaded onto a size exclusion column (HiLoad 16/600 Superdex 200 prep grade, GE Healthcare). Protein was eluted in pH 7.3 buffer containing 50 mM NaH₂PO₄, 100 mM NaCl, and 2 mM EDTA. Protein purity was >90% on the basis of SDS-PAGE gel electrophoresis and Coomassie staining. Pooled fractions were concentrated, flash frozen in liquid nitrogen, and stored at -80°C. Protein concentration was quantified using Pierce BCA Protein Assay Kit.

Recombinant expression and purification of CypA E81S/K82R, CypB E121S, CypE (131–301) K212A, K217A, and K218A mutants. CypA, CypB, and CypE mutants were purified in a similar manner to wild-type with modification as indicated (see Supplementary Table 5 for expression plasmids). Following initial nickel affinity chromatography and overnight dialysis with thrombin-mediated His₆-tag cleavage, the remaining protein was again run over a Ni(II)-affinity chromatography column (HiTrap FF, GE Healthcare) and flow-through and wash were collected to remove any unbound protein and His₆ tags. Protein purity in flow-through and wash was >95% on the basis of SDS-PAGE gel electrophoresis and Coomassie staining. Pooled flow-through and wash was concentrated, flash frozen in liquid nitrogen, and stored at -80°C. Protein concentration was quantified using Pierce BCA Protein Assay Kit.

In vitro selection of a 256,000-member DNA-templated library with human His₆-CypD. The selection protocol utilized a 256,000-member library and recombinant Ni-NTA beads (DynaBeadsHis-Tag Isolation and Pulldown, Invitrogen) (25 μL) were immobilized on a MagJET Separation Rack (ThermoFisher) with the supernatant subsequently removed. Beads were washed twice with 300 μL of 50 mM sodium phosphate pH 8.0, 300 mM NaCl, 0.01% Tween-20, 2 mM TCEP (Tris(2-carboxyethyl)phosphine) (PBST). Forty micrograms of CypD protein was loaded onto solid support in 300 μL PBST, incubated on rotary for 1 h at 4°C, and washed twice with 200 μL of 50 mM Tris-HCl pH 8.0, 150 mM NaCl, 0.05% Tween-20, 2 mM TCEP (TBST). Immobilized protein was suspended in 100 μL blocking buffer (TBST + 0.1 mg mL⁻¹ bovine serum albumin + 0.6 mg mL⁻¹ yeast total RNA) for 25 min at 4°C. After supernatant was removed, 20 pmol second-generation 256,000-member DTS library was suspended with bead immobilized protein in 50 μL blocking buffer and incubated for 1 h at 4°C. Supernatant was removed (FT fraction) and beads were washed three times with TBST, retaining the supernatants (W1, W2, W3). CypD was eluted off Ni-NTA beads by incubating with 50 μL PBST supplemented with 300 mM imidazole (Elution Buffer) for 5 min. The elution was PCR amplified and barcoded with Illumina Primers as previously reported⁴⁸. PCR amplicons were purified by PAGE, extracted, and quantified with KAPA quantitative PCR analysis and QuBit (Invitrogen). High-throughput DNA sequencing was performed on an Illumina MiSeq according to the manufacturer's instructions for sample preparation. Reads generated were analyzed using the Python scripts (shared in Supplementary Note 1 of Supplementary Information) to quantify library barcodes and calculate change in percentage abundance for each library member compared to the pre-selection library.

Chymotrypsin coupled prolyl-isomerase assay. Adapting a previously described protocol⁴, with an Agilent Bravo Velocity 11 with a 384ST head, 90 μL assay buffer (25 mM HEPES pH 7.3, 100 mM NaCl, 0.01% Triton X-100) containing 5.28 nM cyclophilin was added into a flat, clear-bottom, black 384-well plate pre-chilled in a Corning CoolBox at 2–3°C. Five microliters of compound pre-dissolved in 5% DMSO/assay buffer was then added to appropriate wells and incubated at 2–3°C for 5 min. Five microliters of 0.5 mM α-chymotrypsin from bovine pancreas (Type II, lyophilized powder, Millipore-Sigma) in 20% 1 mM HCl/Assay Buffer was then added to each well and incubated at 2–3°C for 5 min. The plate was then quickly transferred to a FLIPR Tetra High-Throughput Cellular Screening System (Molecular Devices). Using the internal liquid handling system of the FLIPR, 1 μL 0.5 mM Suc-AAPF-AMC (Chymotrypsin Substrate II, Millipore-Sigma) dissolved in 0.55 M LiCl/2,2,2-trifluoroethanol was added to each well, which was then mixed for 5 s, followed by immediate fluorescence measurements every 1 s for 330 s using a 360–380 nm excitation LED module and a 400–460 nm emission filter. Final concentrations of the plate include 5 nM cyclophilin, 0.25% DMSO, 25 μM α-chymotrypsin, 5 μM Suc-AAPF-AMC. Raw fluorescence data was analyzed by non-linear regression analysis with Prism v.9 by fitting one-phase association curves to each well. Analyses were halted after the calculated maximum fluorescent value owing to observed fluorescent bleaching during the sustained fluorescent plateau. Rate constants calculated for each well (s⁻¹) were then normalized to substrate only (no prolyl-isomerase) and enzyme + substrate only controls. IC₅₀

values were calculated as the value at which 50% inhibition was achieved on the non-linear regression fitted curve of each compound.

Anisotropy binding assay. Adapted from previous work⁵², titrated cyclophilin in assay buffer (25 mM HEPES pH 7.3, 100 mM NaCl, 0.01% Triton X-100) was incubated with 0.5 nM fluorescein-labeled macrocycle for 6 h at room temperature in a flat-bottom black untreated 96-well plate (Corning). Final assay volume was 100 μL with 0.25% DMSO. Fluorescence anisotropy was then measured using a Tecan Spark plate reader using 492 nm/523 nm excitation/emission settings. Raw fluorescence polarization data was analyzed by non-linear regression analysis with Prism v.9.3.1 by fitting to a one site-total binding equation, providing a dissociation constant (K_D) for each cyclophilin–compound pair.

Competitive anisotropy binding assay with A26-FI. Adapted from previous work⁵², cyclophilin in assay buffer (25 mM HEPES pH 8.0, 100 mM NaCl, 0.01% Triton X-100) at a pre-determined concentration from Supplementary Table 6 was incubated with 0.5 nM A26-FI for 10 min at room temperature in a flat-bottom black untreated 96-well plate (Corning). Competitor macrocycle was then added to each well and incubated for 24 h. Final assay volume was 100 μL with 0.25% DMSO. Fluorescence anisotropy was then measured using a Tecan Spark plate reader using 492 nm/523 nm excitation/emission settings. Raw fluorescence polarization data was normalized to protein + fluorescent probe (0%) and buffer + fluorescent probe (100%) and K_i values were calculated using one site-competitive binding equation with Prism v.9.3.1, importing K_D values from A26-FI (Extended Data Fig. 7).

Surface plasmon resonance analysis of CypD ligands. Adapting a previously used protocol⁵³, employing a Biacore T200 SPR, a Sensor 5 NTA (Biacore) chip was pre-loaded with 0.3 M NiCl₂ and His₆-CypD (50.24 nM, 1 μg mL⁻¹) within a solution of 10 mM HEPES, 150 mM NaCl, 0.005% Tween-20 and 1 mM TCEP (surface plasmon resonance (SPR) buffer). Protein was covalently immobilized subsequently with injection of 200 mM 1-ethyl-3-(3-dimethylaminopropyl) carbodiimide (EDC) 50 mM N-hydroxysuccinimide (NHS). EDC-NHS-activated chip was quenched by flowing 1 M ethanolamine over the chip. Compounds were dissolved in 1% DMSO/SPR buffer and flowed over the SPR chip. Binding analysis was conducted from raw sensorgram resonance unit (RU) values, where individual replicates represent kinetic fitted RU value during time of compound administration at each dose. RU values were normalized to DMSO treatment and the maximum RU value of 200 μM JOMBt. These values were evaluated using Prism v.9 by fitting one site-specific binding to calculate K_D values.

Assessment of covalent modification of CypE and other cyclophilin proteins. In PCR strips, CypE or other cyclophilin in assay buffer (25 mM HEPES pH 8.0, 100 mM NaCl, 0.01% Triton X-100) was incubated with compound for 1 h at room temperature. Final concentrations were 20 μM CypE, 100 μM compound, 0.5% DMSO, at a final volume of 20 μL. For analysis of lysine-iminoboronate modification, samples were directly submitted to Harvard's Center for Mass Spectroscopy for LC-MS analysis. For amine-lysine modification, samples were treated with 5 μL of 125 mM sodium cyanoborohydride dissolved in 25 mM ammonium bicarbonate solution (pH 8.0) and incubated for 4 h at room temperature. For all other wild-type cyclophilins, protein was treated for 4 h with CSA, followed by 16 h treatment with NaCNBH₃. The final concentration of NaCNBH₃ was 25 mM. Samples were then submitted for LC-MS as described above.

Co-crystallization of CypD K175I PPI domain (45–207) with macrocycle compounds. Macrocycles were incubated with 15 mg mL⁻¹ CypD K175I (45–207) (JOMBt, B1, B2, B3 at 1:3; A26 at 1:1.5; B21, B23, B25, B52, B53 at 1:2) for 15 min on ice. Crystals were obtained by mixing 1 μL of the protein–drug complex with 1 μL mother liquor (JOMBt: 19% PEG 3350, 0.5 M KH₂PO₄ pH 7.3; A26: 29% PEG 3350, 0.5 M KH₂PO₄ pH 7.3; B1: 23% PEG 3350, 0.5 M KH₂PO₄ pH 7.3; B2: 28% PEG 3350, 0.5 M KH₂PO₄ pH 7.3; B3: 28% PEG 3350, 0.5 M KH₂PO₄ pH 7.3; B21: 20% PEG 3350, 0.5 M KH₂PO₄ pH 7.3; B23: 21% PEG 3350, 0.5 M KH₂PO₄ pH 8.2; B25: 13% PEG 3350, 0.5 M KH₂PO₄ pH 8.0, 7.5% glycerol; B52: 15% PEG 3350, 0.5 M KH₂PO₄ pH 6.0, 1 mM NaCl; B53: 22.5% PEG 3350, 0.5 M KH₂PO₄ pH 6.0, 1 mM NaCl) and equilibrating against 1 mL of the same reservoir solution at room temperature. Large single rectangular crystals formed within 24 h and were equilibrated in a cryoprotective crystallography buffer composed of mother liquor containing 30% glycerol then snap frozen in liquid nitrogen. Diffraction data was collected from single crystals at 100 K at the FMX (CypD–JOMBt: λ = 0.97933 Å; CypD–A26: λ = 0.97933 Å; CypD–B1: λ = 0.97933 Å; CypD–B2: λ = 0.97933 Å; CypD–B3: λ = 0.97933 Å; CypD–B21: λ = 0.92016 Å; CypD–B23: λ = 0.97931 Å) and the AMX (CypD–B25: λ = 0.92011 Å; CypD–B52: λ = 0.92011 Å; CypD–B53: λ = 0.92011 Å) beamlines at the National Synchrotron Light Source II operated by Brookhaven National Laboratory at the indicated wavelengths.

Crystal structure refinement. Diffraction data for JOMBt, A26, B1, B2, and B3 was indexed, integrated, and scaled with autoPROC, and diffraction data for B21, B23, B25, B52, and B53 was indexed, integrated, and scaled with FastDP. Both programs rely on additional functionality within XDS and CCP4. Phases were assigned via molecular replacement in Phaser⁵⁴ with the apo structure of CypD

K175I (PDB ID 2BIT) for CypD–JOMBt and subsequently with our previously solved structures of CypD K175I complexed with macrocyclic inhibitors as the search model. All refinements to the model were made in PHENIX⁵⁵. Model building was performed in Coot⁵⁶ with ligands and waters fit into the initial $[F_o - |F_c|]$. Macrocyclic restraints were generated using eLBOW (JOMBt, A26, B1, B2, B3) and the ProDrg server⁵⁷ (B21, B23, B25, B52, B53). The coordinates of the holo-structures of CypD have been deposited in the PDB. Additional crystallographic and data collection statistics are listed in Supplementary Table 9. Ligand electron densities are displayed in Supplementary Fig. 34.

Molecular footprinting analysis. Molecular footprints, defined as per-residue decomposition of the Van der Waals, electrostatic, and hydrogen bonding energies between the ligand and the receptor, were generated with the crystal structures in the DOCK6.9 molecular modeling software as described by Balius et al.⁵⁸ In brief, two crystal structures were structurally superimposed in UCSF Chimera on the basis of lowest pairwise root-mean square deviation using the Needleman–Wunsch alignment algorithm. Both the reference ligand and B52 were saved in relation to the CypD–B52 protein structure and were parameterized using the GAFF force field and the Gasteiger charging method. The ligands were then rigidly docked into the receptor using DOCK6.9, and the pairwise interaction energies for the top fifty contributing residues were visualized using matplotlib in Python.

Ligand morph movie. The video morphing between the crystal structures of CypD K175I in its apo state (PDB: 2BIT) through JOMBt, A26, B2, B23, and B52 was made in the molecular visualization software suite UCSF Chimera⁵⁹. The six structures were structurally superimposed on the basis of lowest pairwise root-mean square deviation using the Needleman–Wunsch alignment algorithm and morphed with corkscrew interpolation at an interpolation rate of 150 steps between each conformation. Each crystallized ligand pose was saved as a separate Mol2 file in relation to the final trajectory structure. The trajectory was visualized with ligands using a per-frame script and recorded forwards and backwards.

Isolation of mouse liver mitochondria. All procedures used in animal studies were approved by the Institutional Animal Care and Use Committee at Massachusetts General Hospital. Female C57BL/6J mice (Jackson Labs) age 10–12 weeks were anesthetized by isoflurane. The liver from one mouse was rinsed in ice-cold PBS, minced in ice-cold isolation buffer containing 0.28 M sucrose, 10 mM Hepes–KOH pH 7.2, 0.2 mM EDTA and 1% (w/v) bovine serum albumin, gently homogenized with four strokes of a tight-fitting Teflon pestle at 1,000 r.p.m., and then centrifuged for 10 min at 600g at 4°C. The supernatant was recovered and centrifuged for 10 min at 8,000g at 4°C. The loose outer buffy coat was rinsed off and the pellet resuspended gently in isolation buffer and the spins were repeated. The remaining buffer coat layer was rinsed off and the pellet resuspended in buffer containing 137 mM KCl, 10 mM Hepes–KOH pH 7.2, 2.5 mM MgCl₂ for a final concentration between 40–80 mg mL⁻¹ as assessed by Bradford. The suspension was kept on ice and all assays performed within 4–6 h following isolation. Quality control was done with every preparation by adding 250 mcg mitochondria to 500 µL assay buffer containing 137 mM KCl, 10 mM Hepes–KOH pH 7.2, 2.5 mM MgCl₂, 5 mM each of glutamate and malate, and 3 mM KH₂PO₄. Sequential 150 µM ADP pulses were then delivered. Only preparations with respiratory control ratio >6 (as assessed by the ratio of ADP-coupled state 3 respiration to state 4 respiration) were used for further experiments. Measurements were made in a custom-built spectrometer.

Mitochondrial calcium retention capacity assays. Two hundred and fifty micrograms of mouse liver mitochondria isolated as above were added to 500 µL assay buffer containing 125 mM KCl, 20 mM Hepes–KOH pH 7.2, 1 mM MgCl₂, 5 mM each of glutamate and malate, and 3 mM KH₂PO₄, 0.5 µM Calcium Green 5N (Molecular Probes) was included to monitor extramitochondrial free Ca²⁺. Fluorescence was continuously monitored in the custom-built fluorimeter described above, with excitation 470 nm and emission 520–560 nm. Sequential 60 µM CaCl₂ pulses were delivered until Ca²⁺ uptake ceased and an abrupt release of previously taken up Ca²⁺ was observed, consistent with mPTP opening. The calcium retention capacity ratio was obtained by normalizing the number of Ca²⁺ pulses that could be taken up in a given condition by that taken up under DMSO control conditions, as previously described⁶⁰. Student's *t*-test was used to determine statistical significance between predefined comparisons (DMSO versus CsA, inactive versus active enantiomers of B52–Cy5, and inactive versus active enantiomers of B53–Cy5).

Fluorescence microscopy on HeLa cells. Cells were seeded into 96-well, black, clear-bottom, TC-treated plates, in DMEM supplemented with 10% FBS 24 h prior at a density where wells were ~80% confluent at the time of the experiment. Medium was removed and cells were then stained with 50 µL mixture containing Cy5-labeled compound (6 µM) in Krebs ringer solution HEPES buffered pH 7.2 (KRB), for 1 h at 37°C. Then, 50 µL Hoechst 33342 (8 µM) and Mitotracker Green FM (0.1 µM) in KRB was added directly to wells containing cells and incubated for 15 min at 37°C. Medium was removed and cells were washed twice with 100 µL KRB. Cells were then kept adherent to the wells in 100 µL KRB for imaging.

Fluorescence microscopy was conducted on an Opera Phenix Plus High-Content Screening System, using Alexa 488, Alexa 647, and Hoescht 33342 channels. Images were analyzed using Harmony v.4.9.

In vitro esterase activity on ester pro-drug Cy5 derivatives of CypD inhibitors. In PCR tubes, ester compound (6 µM) and either buffer only, CES1 (0.25 µM), or CES2 (0.25 µM) was diluted in 100 mM Tris–HCl buffer, pH 7.4, with a final DMSO concentration of 1%. Samples were maintained on a PCR block at 37°C for 8 h. After incubation, samples were diluted with 20 µL acetonitrile and analyzed by LC–MS at Harvard's Center for Mass Spectroscopy. Di-ester, mono-ester, and di-acid abundances were quantified by total ion count of the primary isotope and the three compounds were summed and each one expressed as a fraction of the total sum.

Cellular esterase activity on ester pro-drug Cy5 derivatives of CypD inhibitors. Cells were seeded in 96-well, clear, flat-bottom, TC-treated plates in DMEM supplemented with 10% FBS for HEK293T, HeLa, and MEFs, F-12K supplemented with 10% FBS for A549, or MEM supplemented with 10% FBS for HepG2. Cells were seeded 24 h prior at a density where wells were ~70% confluent at the time of the experiment. Medium was removed and cells were incubated with 100 µL mixture containing each Cy5-conjugated compound (6 µM) in their respective medium at 1% DMSO for 48 h (36 h for HepG2) at 37°C at 5% CO₂. Supernatant was removed, and cells were washed twice with 100 µL PBS pH 7.4 (Gibco). Cells were then lysed for 15 min with 30 µL 10 mM Tris–HCl pH 8.0 buffer containing 0.05% SDS. Lysates were diluted with 100 µL acetonitrile and filtered. Lysates were analyzed by LC–MS at Harvard's Center for Mass Spectroscopy. Di-ester, mono-ester, and di-acid abundances were quantified by total ion count of the primary isotope, and the three compounds were summed and each one expressed as a fraction of the total sum.

paxdb⁴¹ quantification of human cyclophilin abundance. Relative human cyclophilin abundances were calculated using paxdb⁴¹, filtered for *Homo sapiens* and the gene identifier of each cyclophilin (Supplementary Table 1). Parts per million values were reported from calculated whole organism (integrated) abundance.

Reporting summary. Further information on research design is available in the Nature Research Reporting Summary linked to this article.

Data availability

High-throughput sequencing data for both replicates of His₆-CypD selection and pre-selection library using a 256,000-member DNA-templated library are available on the NCBI Sequence Read Archive under accession PRJNA797008. The X-ray co-crystal structures of CypD–JOMBt, CypD–A26, CypD–B1, CypD–B2, CypD–B3, CypD–B21, CypD–B23, CypD–B25, CypD–B52, CypD–B53 are available on the PDB (IDs 7TGS, 7TGT, 7TGU, 7TGV, 7TH1, 7TH6, 7TH7, 7THC, 7THD, 7THE, respectively). The CypD + CsA co-crystal structure used is PDB 2Z6W. Human cyclophilin abundance was calculated using paxdb⁴¹ (<https://www.pax-db.org>). Source data are provided with this paper.

Code availability

Custom python scripts for analyzing selection data are provided in Supplementary Note 1 within the Supplementary Information. UCSF DOCK6.9 was used for molecular footprinting analyses. Crystal structures solved using the Phenix Software Suite (v.1.171-3660). Structures analyzed in PyMOL (v.2.5.2) and UCSF Chimera (v.1.16).

References

- Schlatter, D. et al. Crystal engineering yields crystals of cyclophilin D diffracting to 1.7 Å resolution. *Acta Crystallogr. D Biol. Crystallogr.* **61**, 513–519 (2005).
- Mori, T. et al. Use of a real-time fluorescence monitoring system for high-throughput screening for Prolyl isomerase inhibitors. *J. Biomol. Screen.* **14**, 419–424 (2009).
- Liu, Y. et al. A fluorescence polarization-based assay for peptidyl prolyl *cis/trans* isomerase cyclophilin A. *Anal. Biochem.* **356**, 100–107 (2006).
- Wear, M. A. et al. A surface plasmon resonance-based assay for small molecule inhibitors of human cyclophilin A. *Anal. Biochem.* **345**, 214–226 (2005).
- McCoy, A. J. et al. Phaser crystallographic software. *J. Appl. Crystallogr.* **40**, 658–674 (2007).
- Liebschner, D. et al. Macromolecular structure determination using X-rays, neutrons and electrons: recent developments in Phenix. *Acta Crystallogr. D Struct. Biol.* **75**, 861–877 (2019).
- Emsley, P., Lohkamp, B., Scott, W. G. & Cowtan, K. Features and development of Coot. *Acta Crystallogr. D Biol. Crystallogr.* **66**, 486–501 (2010).
- Schüttelkopf, A. W. & van Aalten, D. M. F. PRODRG: a tool for high-throughput crystallography of protein–ligand complexes. *Acta Crystallogr. D Biol. Crystallogr.* **60**, 1355–1363 (2004).

58. Balias, T. E., Mukherjee, S. & Rizzo, R. C. Implementation and evaluation of a docking-rescoring method using molecular footprint comparisons. *J. Comput. Chem.* **32**, 2273–2289 (2011).
59. Pettersen, E. F. et al. UCSF Chimera—a visualization system for exploratory research and analysis. *J. Comput. Chem.* **25**, 1605–1612 (2004).
60. Carroll, J., He, J., Ding, S., Fearnley, I. M. & Walker, J. E. Persistence of the permeability transition pore in human mitochondria devoid of an assembled ATP synthase. *Proc. Natl Acad. Sci.* **116**, 12816–12821 (2019).

Acknowledgements

This work was supported by NIH R35 GM118062 (D.R.L.), R01 EB022376 (D.R.L.), R35 GM119437 (M.A.S.), S10 OD028478 (M.A.S.), F30 CA260772 (A.M.R.), T32 GM008444 (A.M.R., I.R.O.), R01 AR071942 (V.K.M.), K08 HL157620 (P.S.W.), and the Howard Hughes Medical Institute (V.K.M., D.R.L.). We thank S. Trauger and J. Wang for assistance with mass spectrometry, which was conducted at Harvard's Center for Mass Spectrometry. We thank S. Mayo, R. Tillman, J. Santos, J. Gale, S. Hoang, and M. Alimova of the Broad Institute's CDOT platform for assistance and use of their instrumentation. We thank N. Elowe for assistance with SPR experiments. X-ray diffraction data was collected at the AMX and FMX beamlines of the Center for BioMolecular Structure (CBMS) at the National Synchrotron Light Source II, a U.S. Department of Energy (DOE) Office of Science User Facility operated for the DOE Office of Science by Brookhaven National Laboratory under Contract No. DE-SC0012704. The CBMS is primarily supported by the National Institutes of Health, National Institute of General Medical Sciences (NIGMS) through a Center Core P30 Grant (P30 GM133893) and the DOE Office of Biological and Environmental Research (KP1605010).

Author contributions

A.A.P. conducted the in vitro selection of the DNA-templated macrocycle library, designed, synthesized, and characterized macrocycles, conducted the in vitro binding

screens, inhibition screens, biochemical analyses for cyclophilin inhibitors, cell culture experiments, and expressed CypD and mutant proteins. A.M.R. and M.K.T. designed constructs and expressed the other cyclophilins, co-crystallized and solved CypD X-ray crystal structures, and generated structure videos. P.S.W. performed isolated mitochondria experiments. C.H. assisted in preparing macrocycles and conducting in vitro screens for the CypE portion of this work. I.R.O. assisted in solving CypD macrocycle X-ray co-crystal structures. A.I.C. conducted the selection of the DNA-templated macrocycle library. D.L.U. assisted in identifying hits from CypD selection. V.K.M. supervised mitochondrial experiments. M.A.S. and D.R.L. supervised the research project. A.A.P., A.M.R., P.S.W., C.H., V.K.M., M.A.S., D.R.L. contributed to the writing of this manuscript.

Competing interests

A.A.P. and D.R.L. are co-inventors on patent applications that are based on this work. D.R.L. is a consultant and co-founder of Exo Therapeutics, a company that uses DNA-encoded libraries and exo-site inhibition.

Additional information

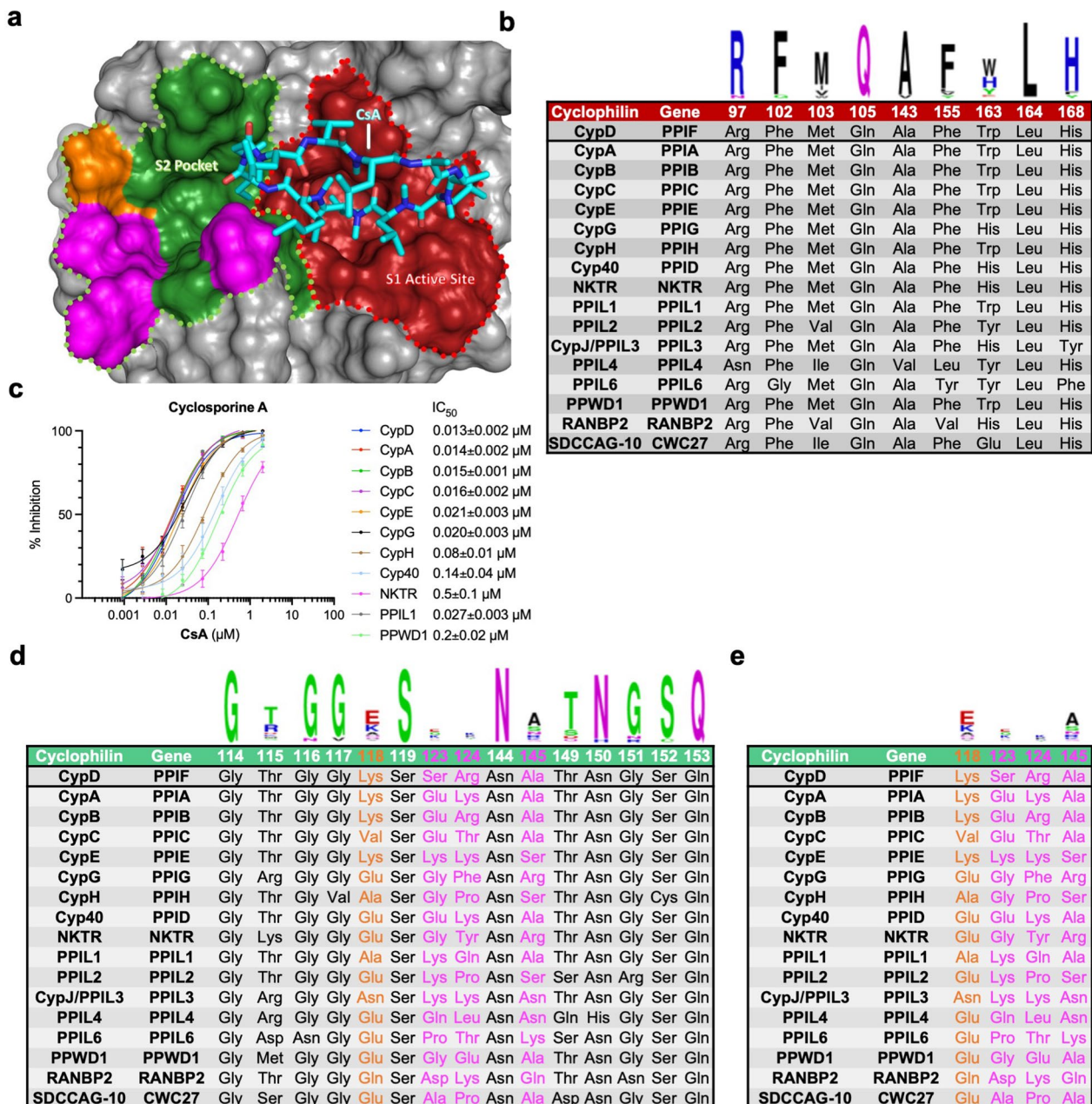
Extended data is available for this paper at <https://doi.org/10.1038/s41589-022-01116-1>.

Supplementary information The online version contains supplementary material available at <https://doi.org/10.1038/s41589-022-01116-1>.

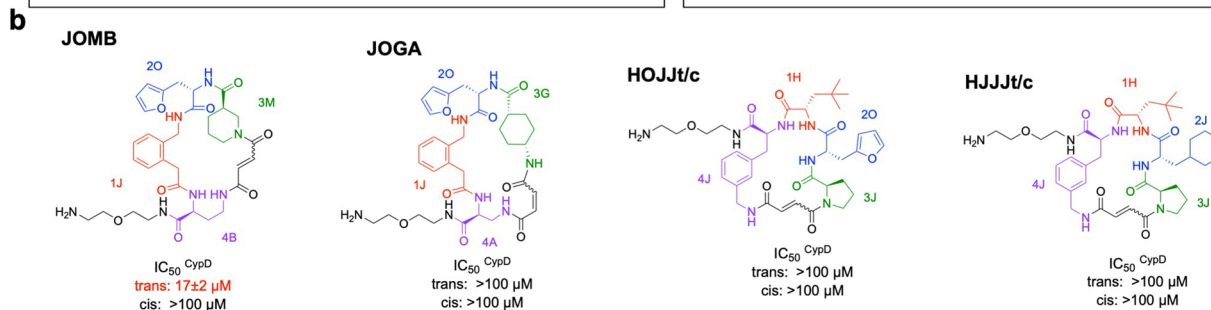
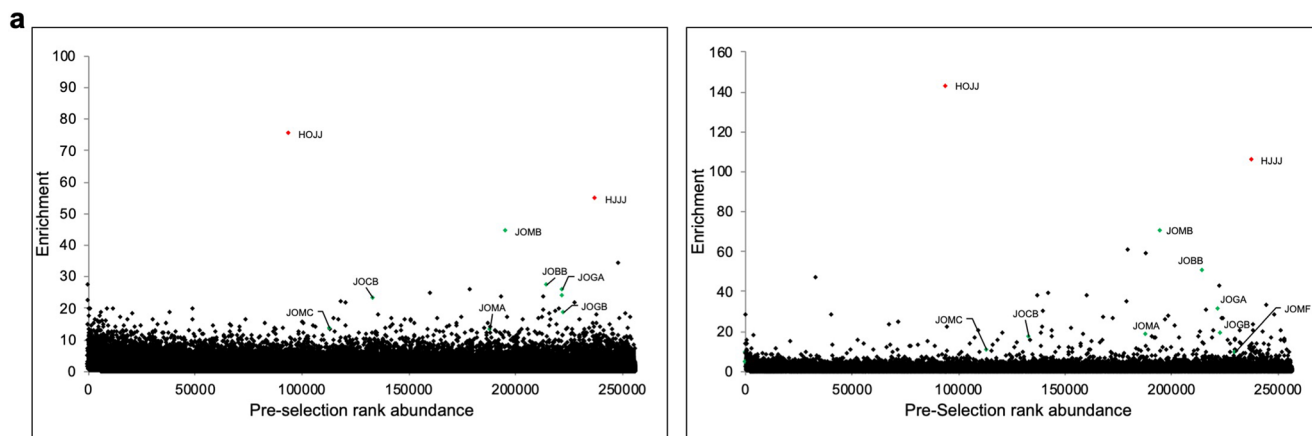
Correspondence and requests for materials should be addressed to Markus A. Seeliger or David R. Liu.

Peer review information *Nature Chemical Biology* thanks Sirano Dhe-Paganon, Paige Dickson, Brian Schultz and the other, anonymous, reviewer(s) for their contribution to the peer review of this work.

Reprints and permissions information is available at www.nature.com/reprints.



Extended Data Fig. 1 | Exclusive active site binding results in promiscuous cyclophilin inhibition. **a**, Co-crystal structure of CsA bound to CypD (PDB ID 2Z6W). CsA (cyan) binds to the active site (red) of CypD, a binding mode that does not engage more diversified residues that lie in the S2 pocket (green), including the primary gatekeepers (magenta) and the semiconserved K118 residue (orange). **b**, Active site (S1 pocket) residues with WebLogo plots, showing high conservation between the 17 cyclophilin isoforms with corresponding gene and protein identifier. **c**, Isomerization of the reporter peptide Suc-AAPF-AMC was measured with 5 nM cyclophilin and varying concentrations of CsA. CsA shows potent, but promiscuous inhibitory activity against all prolyl isomerase-active cyclophilins. Selective inhibition could rather be achieved through interactions with S2 pocket residues of cyclophilin subtypes (**d**). **e**, Cyclophilin S2 pocket residues that are the primary diversification sites within the active site-S2 pocket groove with WebLogo plots. Typical cyclophilin inhibitors such as CsA do not engage in interactions with these residues. All residue numbering is in reference to CypD. IC₅₀ values reflect mean ± s.e.m. of three technical replicates. Data points and error bars reflect mean ± s.d. of individual assays at one dose.



c

Compound	1st building block	IC ₅₀ CypD
A1		>100 μM
A2		>100 μM
A3		>100 μM
A4		>100 μM
A5		>100 μM
A6		>100 μM

Compound	2nd building block	IC ₅₀ CypD
A7		>100 μM
A8		>100 μM
A9		17±8 μM
A10		>100 μM
A11		17±4 μM
A12		>100 μM
A13		>100 μM
A14		3.8±0.9 μM
A15		18±3 μM
A16		>100 μM
A17		14±3 μM
A18		>100 μM
A19		22±3 μM
A20		10±2 μM

Compound	3rd building block	IC ₅₀ CypD
JOBBt JOBbC-A		trans: 45±6 μM cis: >100 μM
JOGBt-A JOGBc-A		trans: >100 μM cis: >100 μM
JOCBt JOCBc		trans: >100 μM cis: >100 μM
A21		>100 μM
A22		13±7 μM
A23		>100 μM
A24		>100 μM
A25		3.6±0.6 μM
A26		0.20±0.02 μM
A27		23±6 μM
A28		10±2 μM
A29		8.2±0.9 μM

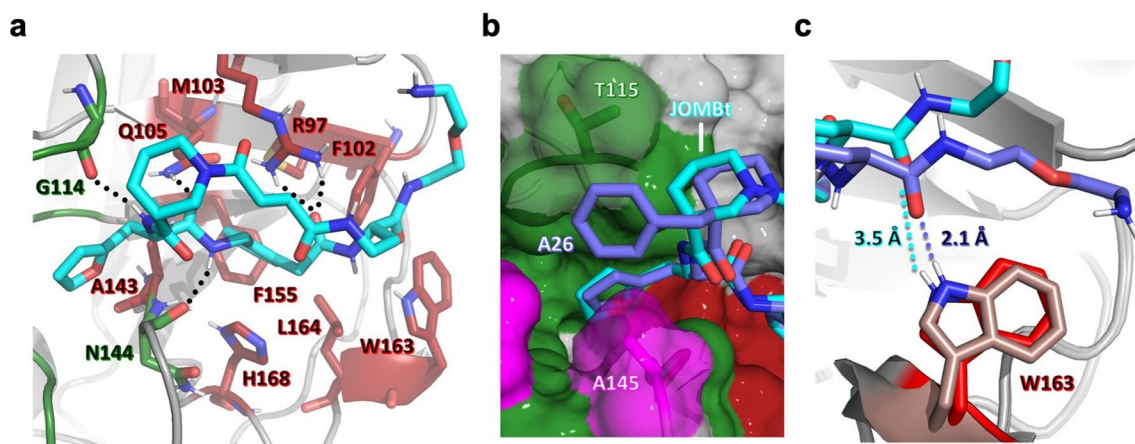
Compound	4th building block	IC ₅₀ CypD
JOMAt JOMAc	Linker Tail	trans: >100 μM cis: >100 μM
JOMCt JOMCc	Linker Tail	trans: >100 μM cis: >100 μM
JOMFt JOMFc	Linker Tail	trans: ~90 μM cis: >100 μM

Compound	Cyclization linker	IC ₅₀ CypD
JOMBc		>100 μM
A30		>100 μM

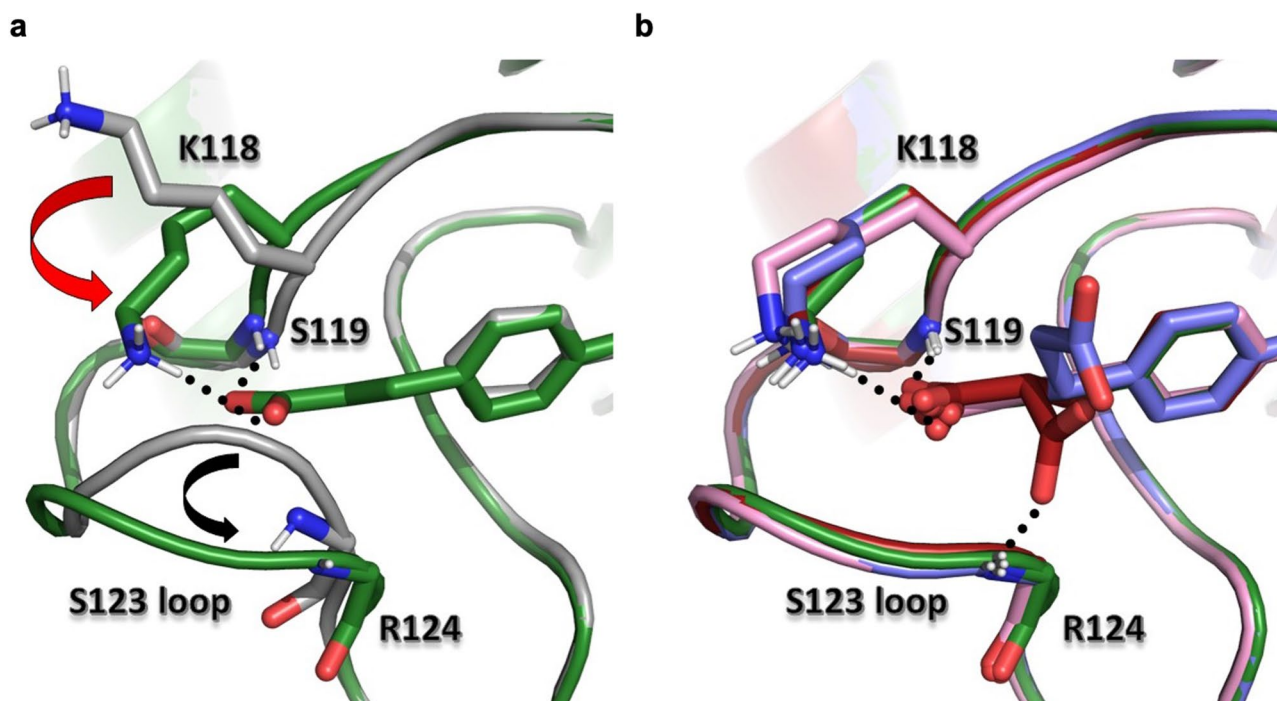
Compound	Tail	IC ₅₀ CypD
JOMBt-A		16±3 μM
JOMBt-D		3.2±0.3 μM

Extended Data Fig. 2 | See next page for caption.

Extended Data Fig. 2 | Overview of macrocycle library hits from the CypD binding selection and JOMBt structure-activity relationships. **a**, Two replicates of this selection yielded consistent enrichment of the JO** family of macrocycles. Library hits re-synthesized in DNA-free form resulted in novel CypD inhibitors JOMBt and JOBBt, the starting points of CypD inhibitors developed in this study. **b**, Structure JOMB, JOGA, and H*JJ macrocycles that enriched well in the DNA-templated macrocycle library selection. JOMB in the trans isomer (JOMBt) exhibits weak prolyl isomerase inhibition. **c**, Library hits and derivatives of JOMBt and their corresponding prolyl isomerase inhibition IC_{50} values for CypD. Each listed compound has the JOMBt structure except for the drawn building block substitution. Note, library encoded macrocycles that denote an '-A' nomenclature (JOGt-A, JOGBc-A, JOBBc-A) include the same primary amide tail shown in JOMBt-A. Values and error bars reflect mean \pm s.e.m. of three technical replicates.



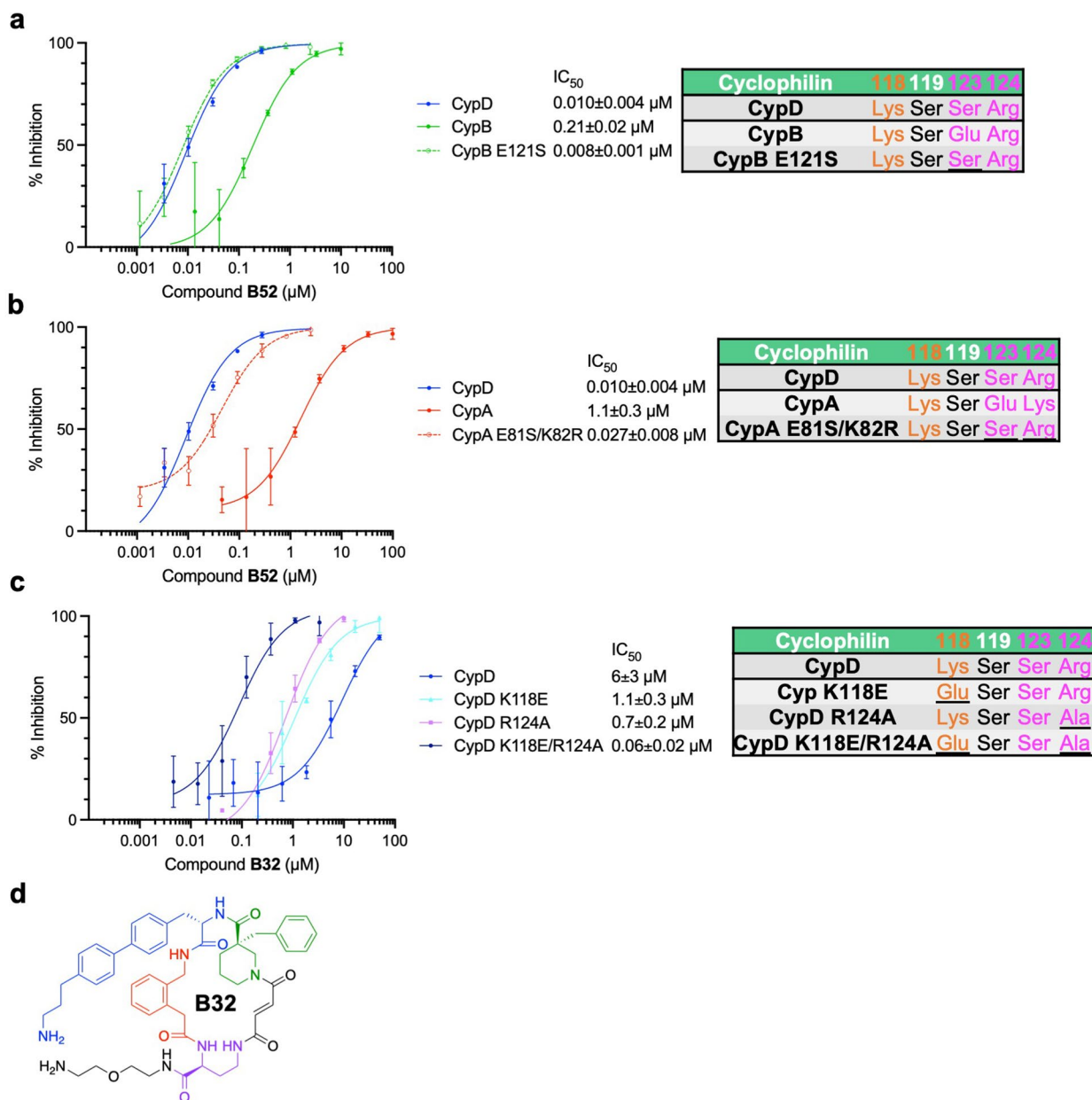
Extended Data Fig. 3 | X-ray co-crystal structure of JOMBt:CypD compared to A26:CypD. **a**, Active site binding pose of JOMBt (PDB ID 7TGS, 1.75 Å resolution) showing almost identical interactions with CypD as A26 (Fig. 1d, e). Black dashes indicate predicted hydrogen bonds. Notable differences between the binding mode of JOMBt and A26 include **b**, An extra hydrophobic contact between the benzyl group of A26 (purple) and T115 (green) is absent with JOMBt (cyan). **c**, An extra hydrogen bond between A26 (purple) and W163 (salmon or red) that JOMBt (cyan) lacks. The W163-JOMBt distance is 3.5 Å (cyan dashes), compared to 2.1 Å for W163-A26 (purple dashes). Van der Waals surfaces of T115 and A145 (magenta) are shown in the structure with A26.



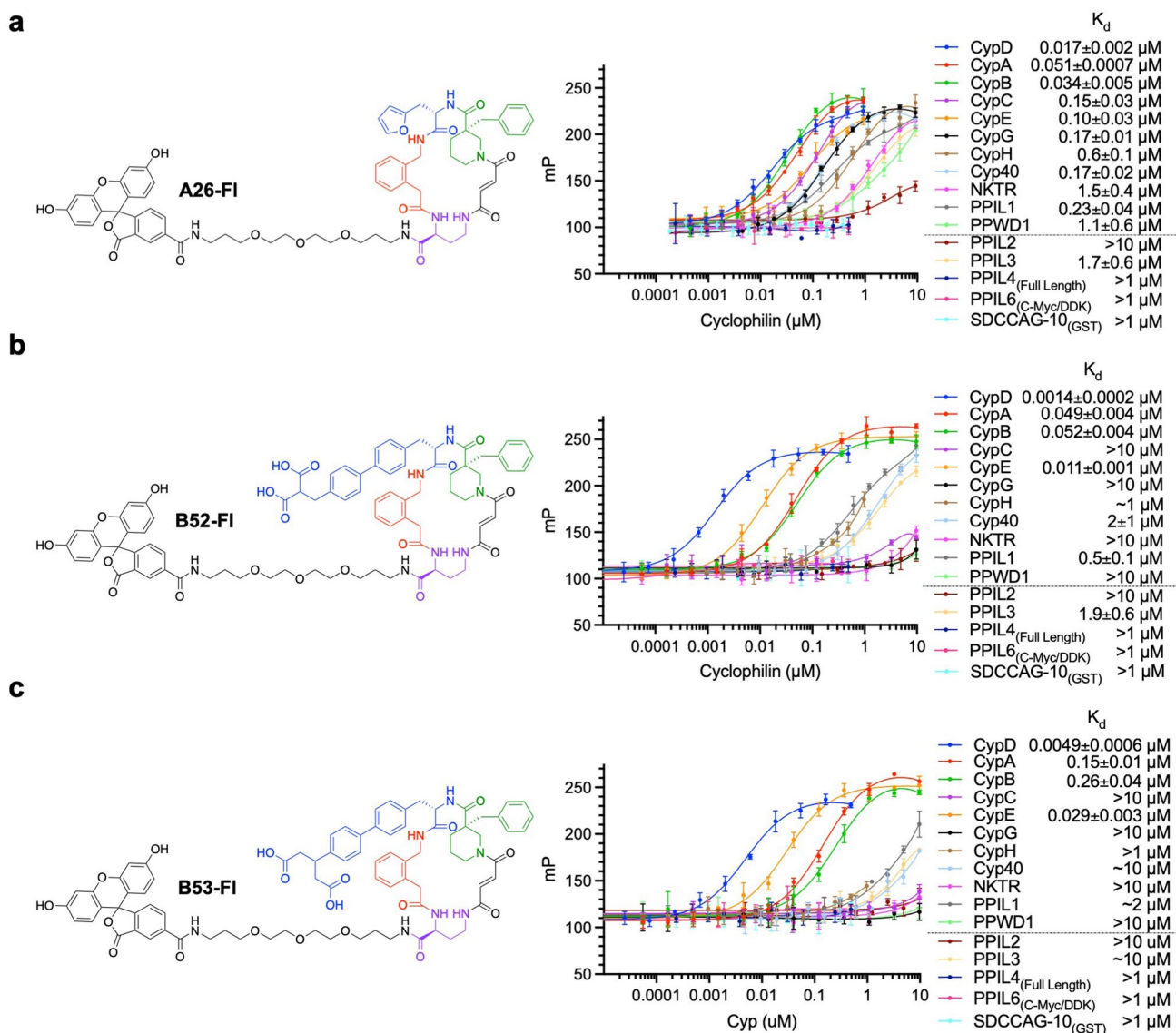
Extended Data Fig. 4 | Carboxylate-containing S2-binding moieties induce K118 side-chain and S123 backbone migration. **a**, Superposition of co-crystal structures of CypD with **B2** (gray) and **B23** (green). The side-chain of K118 typically is oriented away from the S2 pocket, as shown in co-crystal structures that do not contain carboxylate ligands, such as that of **B2**. A properly placed carboxylate group (**B23**) migrates K118's side-chain into the S2 pocket (red arrow), forming a salt bridge along with a hydrogen bond with S119's peptide backbone (black dashes). Also shown is the S123 loop migration that occurs when carboxylate-containing biphenyl groups bind deep into the S2 pocket (black arrow). **b**, Co-crystal structure superposition of CypD with **B23** (green), **B25** (pink), **B52** (red) and **B53** (purple). All properly placed carboxylate-containing ligands induce the same K118 and S123 conformational change. Dicarboxylates such as **B52** and **B53** also present the second carboxylate towards the S123 gatekeeper residue, the former exhibiting a hydrogen bond (black dashes) with the S123-R124 peptide backbone.

CsA IC ₅₀ (normalized IC ₅₀)	B2 IC ₅₀ (normalized IC ₅₀)	B23 IC ₅₀ (normalized IC ₅₀)	B52 IC ₅₀ (normalized IC ₅₀)	B53 IC ₅₀ (normalized IC ₅₀)	Cyclophilin (proximal unique residues)	Binding hypothesis
13 nM (1x)	180 nM (1x)	7.8 nM (1x)	10 nM (1x)	57 nM (1x)	CypD (Lys, Ser, Arg)	H-bond with semiconserved Lys, dicarboxylate tolerated by Ser/Arg gatekeepers
21 nM (1.6x)	300 nM (1.6x)	19 nM (2.4x)	310 nM (31x)	800 nM (14x)	CypE (Lys, Lys, Lys)	H-bonds with semiconserved Lys, but Lys less tolerated sterically by dicarboxylate containing ligand (B52, B53)
15 nM (1.1x)	160 nM (0.9x)	22 nM (2.8x)	210 nM (21x)	1,100 nM (19x)	CypB (Lys, Glu, Arg)	H-bonds with semiconserved Lys, but charge repulsion between Glu gatekeeper and dicarboxylate containing ligand (B52, B53)
14 nM (1.1x)	240 nM (1.3x)	80 nM (10x)	1100 nM (110x)	3,400 nM (60x)	CypA (Lys, Glu, Lys)	
27 nM (2.1x)	1900 nM (11x)	130 nM (17x)	6,000 nM (600x)	>50,000 nM (750x)	PPIL1 (Ala, Lys, Gln)	No Lys for salt bridge to carboxylate ligand (B23) and Lys less tolerated sterically by dicarboxylate ligand (B52, B53)
140 nM (11x)	260 nM (1.4x)	1,700 nM (220x)	22,000 nM (2,200x)	>50,000 nM (>900x)	Cyp40 (Glu, Glu, Lys)	Glu or Val replacing semiconserved Lys resulting in charge or hydrophobic repulsion, charge repulsion at Glu gatekeeper with a carboxylate containing ligand (B23, B52, B53)
16 nM (1.2x)	380 nM (2.1x)	5,000 nM (640x)	>100,000 nM (>10,000x)	>50,000 nM (>900x)	CypC (Val, Glu, Thr)	
20 nM (1.5x)	37,000 nM (210x)	5,000 nM (640x)	>100,000 nM (>10,000x)	>50,000 nM (>900x)	CypG (Glu, Gly, Phe)	Sterically occluded S2 pocket, high (-) charged S2 pocket, or inflexible loop-gatekeeper region. Biphenyl group on ligand alone provides good selectivity over these cyclophilins (B2, B23, B52, B53)
200 nM (15x)	3,200 nM (18x)	11,000 nM (1,400x)	>100,000 nM (>10,000x)	>50,000 nM (>900x)	PPWD1 (Glu, Gly, Glu)	
80 nM (6x)	100,000 nM (560x)	~30,000 nM (>3,800x)	>100,000 nM (>10,000x)	>50,000 nM (>900x)	CypH (Ala, Gly, Pro)	
500 nM (38x)	100,000 nM (560x)	>100,000 nM (>13,000x)	>100,000 nM (>10,000x)	>50,000 nM (>900x)	NKTR (Glu, Gly, Tyr)	

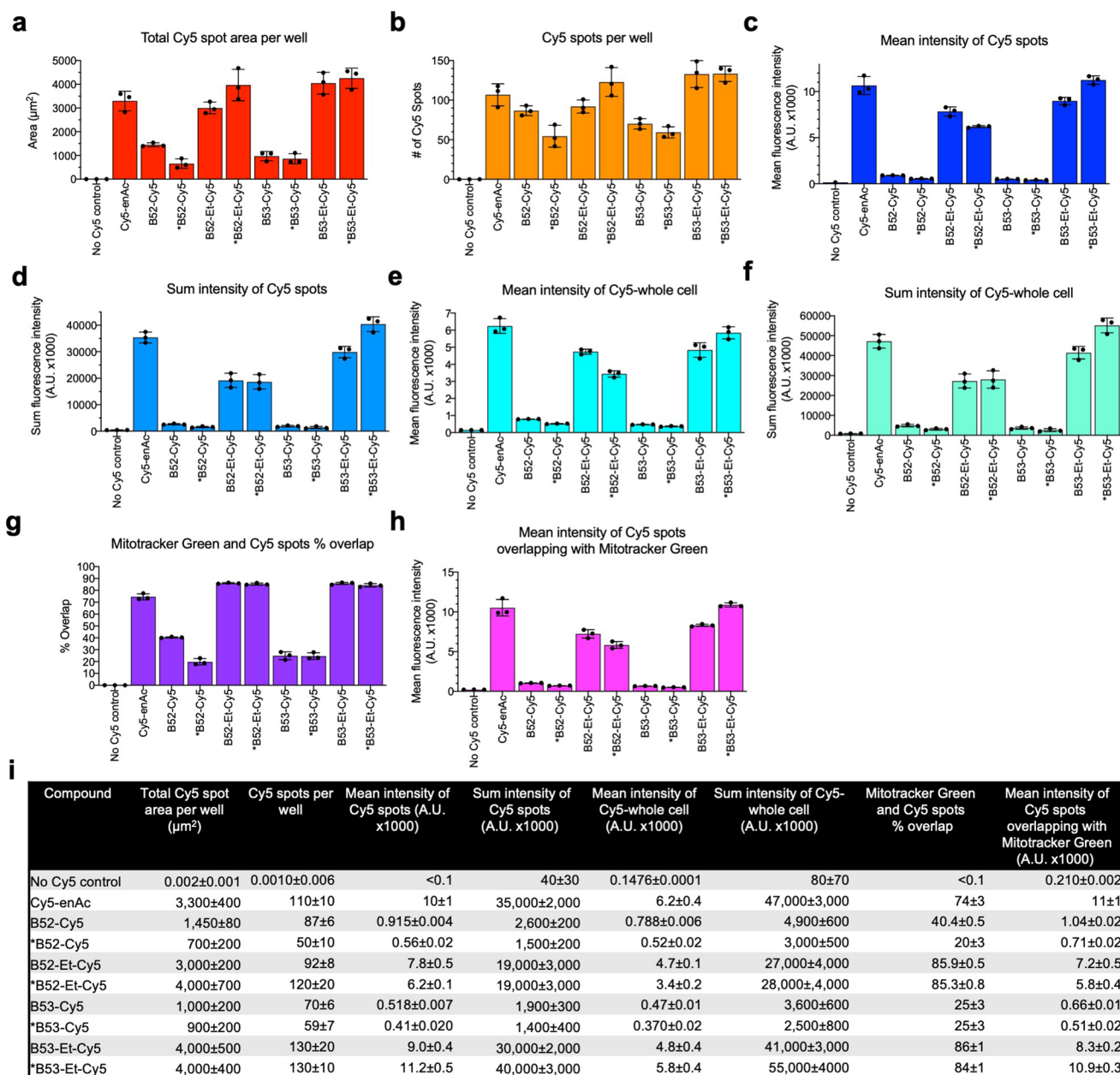
Extended Data Fig. 5 | Analysis of CypD-selective prolyl isomerase inhibition based on S2 pocket containing residues. IC₅₀ values for each cyclophilin are accompanied by fold difference normalized to IC₅₀^{CypD}. Residues listed next to each cyclophilin are the important proximal residues near the carboxylate-containing ligands. CsA does not bind the S2 pocket and shows almost no cyclophilin isoform selectivity, while **B2**'s large biphenyl group exhibits selectivity over cyclophilins with sterically occluded S2 pockets. Further selectivity over CypC, Cyp40, and PPIL1 is achieved through interactions between CypD's K118 residue and carboxylate-containing ligands such as **B23**. Installation of dicarboxylates in **B52** and **B53** result in CypD selectivity by presenting a second carboxylate near the analogous S123 position on CypD. Potency for CsA, **B2**, and **B23** values reflect mean of three technical replicates. Potency for **B52** and **B53** values reflect mean of four independent replicates.



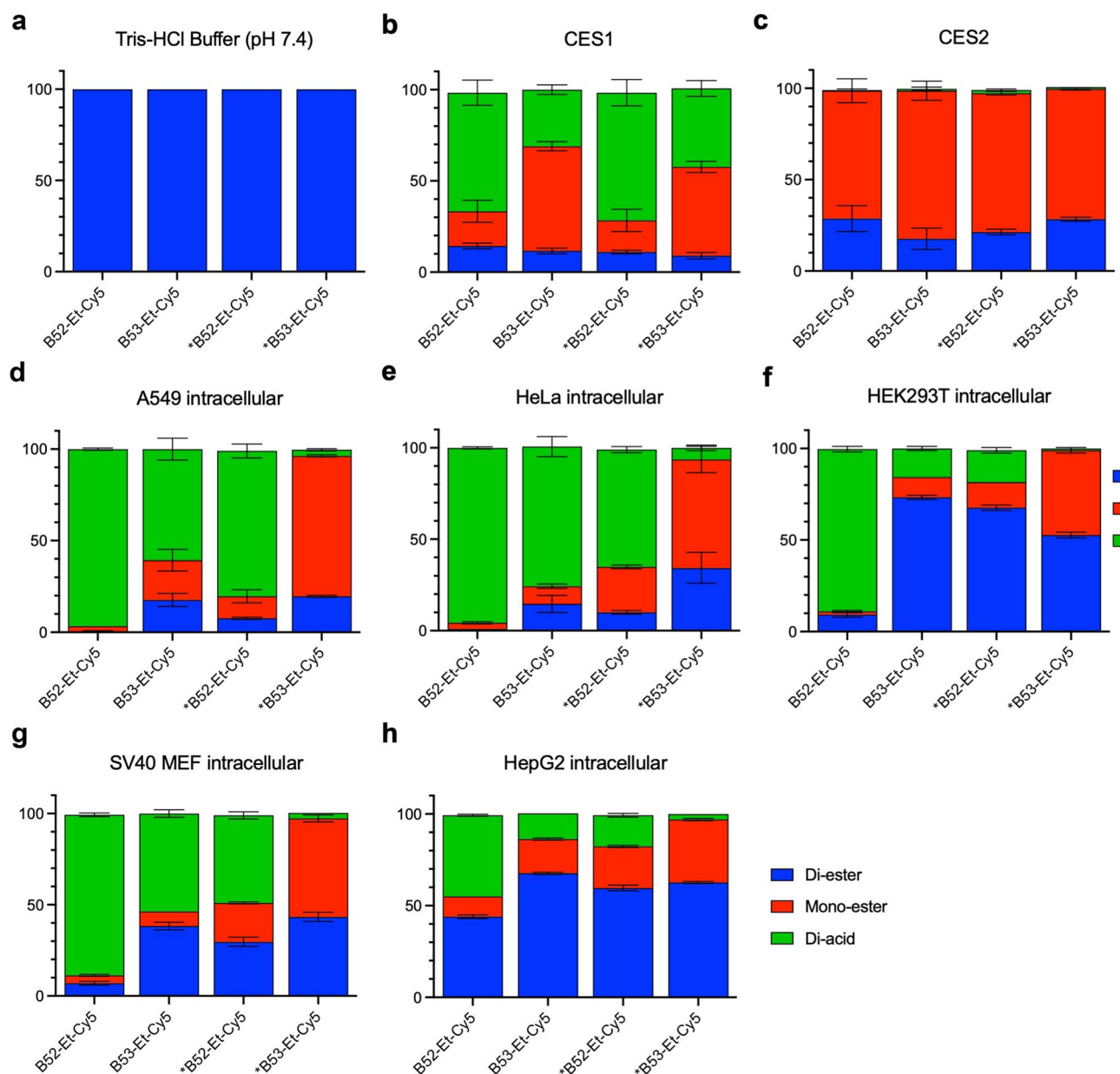
Extended Data Fig. 6 | Inhibition potency is dependent on favorable interactions with S2 pocket residues. Dose response curves for **B52** against **a**, CypB E121S mutant and **b**, CypA E81S/K82R double mutant, with residue tables for important dicarboxylate proximal residues. Mutated residues are underlined. **B52** inhibits both CypB and CypA mutants that have the appropriate 'CypD' gatekeeper residues at similar potency values compared to wild-type CypD. **c**, Dose response curves for **B32** against wild-type CypD and CypD mutants shown in the table. Two mutations to remove positively charged residues K118 and R124 restore inhibition potency of amine derivative **B32**. **d**, Structure of **B32**. For CypD, CypA, and CypB wild-type IC₅₀ data with **B52**, values reflect mean ± s.d. of four independent replicates (each comprising three technical replicates). Graphs show a representative single independent replicate (Independent replicate 1 is shown, containing three technical replicates) with data points and error bars reflecting mean ± s.d. of individual assays at one dose. Further independent replicates are shown in Supplementary Fig. 18b-c. All other IC₅₀ values reflect mean ± s.e.m. of three technical replicates, with data points and error bars reflecting mean ± s.d. of individual assays at one dose.



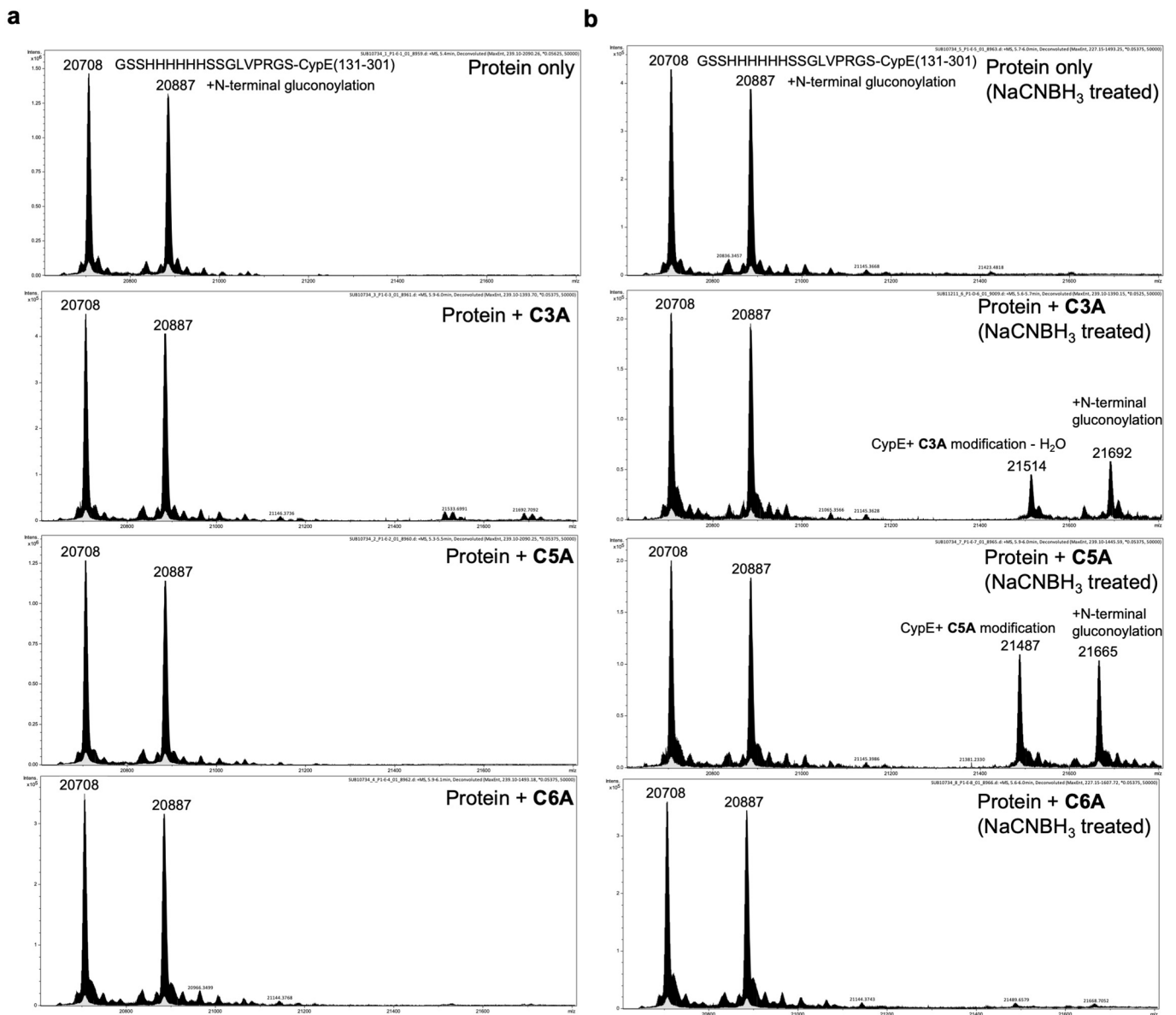
Extended Data Fig. 7 | Cyclophilin binding profiles using fluorescence polarization of fluorescein-labeled macrocycles. Each cyclophilin was titrated against 0.5 nM fluorescein-labeled macrocycle **a**, **A26-FI**; **b**, **B52-FI**; or **c**, **B53-FI**. Trends for selectivity follow those observed in the prolyl-isomerase assay. Cyclophilins in the legend below the dashed line are either prolyl-isomerase inactive or require much higher concentrations to observe prolyl isomerization *in vitro*. K_d values and error bars reflect mean \pm s.e.m. of three technical replicates. Data points and error bars reflect mean \pm s.d. of individual assays at one dose.



Extended Data Fig. 8 | Quantification of mitochondrial localization in HeLa cells by fluorescence microscopy of Cy5-conjugated compounds. HeLa cells were treated with Cy5-conjugated compounds and analyzed for **a**, total identifiable Cy5 spots; **b**, Cy5 spots per well; **c**, mean fluorescence intensity of identified Cy5 spots; **d**, sum of fluorescence intensity of identified Cy5 spots; **e**, mean Cy5 fluorescence intensity per cell; **f**, sum of Cy5 fluorescence in all measured cells; **g**, percent of Cy5 spots that overlap >70% with Mitotracker Green co-stain; and **h**, fluorescence intensity of Cy5 spots that overlap >70% with Mitotracker Green. **i**, values of data shown in **a-h**. Values and error bars reflect mean \pm s.d. of three technical replicates.



Extended Data Fig. 9 | Hydrolysis of ester prodrug CypD inhibitors. Compounds were evaluated for their ability to be hydrolyzed from di-ester to mono-ester, or to di-acid CypD inhibitors. Each reaction was analyzed by LC-MS, and ion abundances for each are shown as a percent of the total sum. These were conducted under conditions of: **a**, Tris-HCl buffer only; **b**, 250 nM carboxylesterase 1 (CES1); **c**, 250 nM carboxylesterase 2 (CES2); **d**, incubated with A549 cells for 48 h and intracellular fraction isolated; **e**, incubated with HeLa cells for 48 h and intracellular fraction isolated; **f**, incubated with HEK293T cells for 48 h and intracellular fraction isolated; **g**, incubated with MEFs for 48 h and intracellular fraction isolated; **h**, incubated with HepG2 cells for 36 h and intracellular fraction isolated. Esters show good stability in buffer and are only cleaved under esterase conditions, or intracellularly, with **B52-Et-Cy5** showing the most rapidly hydrolyzed esters. Values and error bars reflect mean \pm s.d. of three technical replicates.



Extended Data Fig. 10 | Mass spectrometry analysis of compounds co-incubated with CypE. a, Mass spectrometry analysis of lysine covalent modification of CypE with **C3A**, **C5A**, and **C6A**. **b**, Mass spectrometry analysis of lysine covalent modification after treatment with NaCNBH₃ to trap the iminoboronate as a reduced lysine-linked secondary amine, highlighting relevant m/z regions. **C3A** and **C5A** show covalent modification (+779 Da and +806 Da, respectively) of CypE after reductive amination with NaCNBH₃.

Reporting Summary

Nature Portfolio wishes to improve the reproducibility of the work that we publish. This form provides structure for consistency and transparency in reporting. For further information on Nature Portfolio policies, see our [Editorial Policies](#) and the [Editorial Policy Checklist](#).

Statistics

For all statistical analyses, confirm that the following items are present in the figure legend, table legend, main text, or Methods section.

n/a Confirmed

- The exact sample size (n) for each experimental group/condition, given as a discrete number and unit of measurement
- A statement on whether measurements were taken from distinct samples or whether the same sample was measured repeatedly
- The statistical test(s) used AND whether they are one- or two-sided
Only common tests should be described solely by name; describe more complex techniques in the Methods section.
- A description of all covariates tested
- A description of any assumptions or corrections, such as tests of normality and adjustment for multiple comparisons
- A full description of the statistical parameters including central tendency (e.g. means) or other basic estimates (e.g. regression coefficient) AND variation (e.g. standard deviation) or associated estimates of uncertainty (e.g. confidence intervals)
- For null hypothesis testing, the test statistic (e.g. F , t , r) with confidence intervals, effect sizes, degrees of freedom and P value noted
Give P values as exact values whenever suitable.
- For Bayesian analysis, information on the choice of priors and Markov chain Monte Carlo settings
- For hierarchical and complex designs, identification of the appropriate level for tests and full reporting of outcomes
- Estimates of effect sizes (e.g. Cohen's d , Pearson's r), indicating how they were calculated

Our web collection on [statistics for biologists](#) contains articles on many of the points above.

Software and code

Policy information about [availability of computer code](#)

Data collection

Illumina Miseq Control software v2.6 was used on the Illumina Miseq sequencers to collect high-throughput DNA sequencing data. Fluorescence microscopy data was collected in Harmony 4.9 using a Opera Phenix Plus High-Content Screening System. FLIPR data was collected using Screen Works Peak Pro v4.2.1. Tecan Spark data was collected using SparkControl v3. Surface plasmon resonance data was collected using Biacore T200 control software v3.2. Relative cyclophilin subtype abundances in homo sapiens were collected using paxdb4.1.

Data analysis

UCSF DOCK6.9 was used for molecular footprinting analyses. Crystal structures solved using the Phenix Software Suite (Ver 1.171-3660). Structures analyzed in PyMOL (Ver 2.5.2) and UCSF Chimera (Ver 1.16). Custom Python scripts used for analyzing high-throughput sequencing data is provided in the supplementary information. Fluorescence microscopy was analyzed in Harmony 4.9. Biochemical data analysis was conducted using Prism 9.3.1. Surface plasmon resonance data was analyzed using Biacore T200 control software v3.2 and Prism 9.3.1.

For manuscripts utilizing custom algorithms or software that are central to the research but not yet described in published literature, software must be made available to editors and reviewers. We strongly encourage code deposition in a community repository (e.g. GitHub). See the Nature Portfolio [guidelines for submitting code & software](#) for further information.

Data

Policy information about [availability of data](#)

All manuscripts must include a [data availability statement](#). This statement should provide the following information, where applicable:

- Accession codes, unique identifiers, or web links for publicly available datasets
- A description of any restrictions on data availability
- For clinical datasets or third party data, please ensure that the statement adheres to our [policy](#)

X-ray structures of CypD in complex with macrocycles JOMBt, A26, B1, B2, B3, B21, B23, B25, B52, and B53 are available in the PDB (PDB IDs 7TGS, 7TGT, 7TGU,

7TGV, 7TH1, 7TH6, 7TH7, 7THC, 7THD, and 7THF, respectively). CypD-CsA co-crystal structure was obtained from PDB (2Z6W). High-throughput sequencing data for both replicates of His6-CypD selection using a 256,000 DNA-templated library are available on NCBI's Sequence Read Archive (SRA) website (Accession: PRJNA797008). Human cyclophilin abundance was calculated using paxdb4.1 (<https://www.pax-db.org>)

Field-specific reporting

Please select the one below that is the best fit for your research. If you are not sure, read the appropriate sections before making your selection.

Life sciences Behavioural & social sciences Ecological, evolutionary & environmental sciences

For a reference copy of the document with all sections, see nature.com/documents/nr-reporting-summary-flat.pdf

Life sciences study design

All studies must disclose on these points even when the disclosure is negative.

Sample size	Sample sizes are indicated in figure captions. For experiments with isolated mouse liver mitochondria, sample size was pre-specified at 3 per group due to availability of laboratory animals and no sample size calculation was performed. The pre-specified sample size was sufficient to arrive at statistically significant and reproducible results. Samples sizes were chosen to be 3 or 4 for in vitro biochemical analysis to achieve statistical significance.
Data exclusions	No data were excluded from the analyses.
Replication	All attempts at replication were successful. For all in vitro biochemical analyses, microscopy, and cellular assays, three technical replicates were used, with four independent experiments for key data. For isolated mitochondria experiments, three independent experiments were performed on three independent days and replication was successful.
Randomization	N/A. All experiments were done in vitro.
Blinding	N/A. All experiments were done in vitro.

Reporting for specific materials, systems and methods

We require information from authors about some types of materials, experimental systems and methods used in many studies. Here, indicate whether each material, system or method listed is relevant to your study. If you are not sure if a list item applies to your research, read the appropriate section before selecting a response.

Materials & experimental systems

n/a	Involved in the study
<input checked="" type="checkbox"/>	<input type="checkbox"/> Antibodies
<input type="checkbox"/>	<input checked="" type="checkbox"/> Eukaryotic cell lines
<input checked="" type="checkbox"/>	<input type="checkbox"/> Palaeontology and archaeology
<input type="checkbox"/>	<input checked="" type="checkbox"/> Animals and other organisms
<input checked="" type="checkbox"/>	<input type="checkbox"/> Human research participants
<input checked="" type="checkbox"/>	<input type="checkbox"/> Clinical data
<input checked="" type="checkbox"/>	<input type="checkbox"/> Dual use research of concern

Methods

n/a	Involved in the study
<input checked="" type="checkbox"/>	<input type="checkbox"/> ChIP-seq
<input checked="" type="checkbox"/>	<input type="checkbox"/> Flow cytometry
<input checked="" type="checkbox"/>	<input type="checkbox"/> MRI-based neuroimaging

Eukaryotic cell lines

Policy information about [cell lines](#)

Cell line source(s)	HEK293T (ATCC CRL-3216), HeLa (ATCC CCL-2), mouse embryonic fibroblasts (MEFs) (ATCC CRL-2991), HepG2 (ATCC HB-8065), and A549 (ATCC CCL-185).
Authentication	Cell lines were authenticated by their suppliers using STR analysis.
Mycoplasma contamination	Cell lines tested negative for mycoplasma.
Commonly misidentified lines (See ICLAC register)	No commonly misidentified cell lines were used in this study.

Animals and other organisms

Policy information about [studies involving animals](#); [ARRIVE guidelines](#) recommended for reporting animal research

Laboratory animals	C57Bl6/J mice, female, 10-12 weeks old. Mice were housed in the MGH Animal Research Facility on a 12-hour light/dark cycle with stable temperature (22°C) and humidity (60%).
Wild animals	No wild animals were used in this study
Field-collected samples	No field collected samples were used in this study.
Ethics oversight	Institutional Animal Care and Use Committee at Massachusetts General Hospital.

Note that full information on the approval of the study protocol must also be provided in the manuscript.